Timing and duration of Archean orogenic gold deposits in the Bourlamaque pluton, Val d'Or mining camp, Abitibi, Canada

Alain Tremblay, Gilles Ruffet, Jérémie Lemarchand

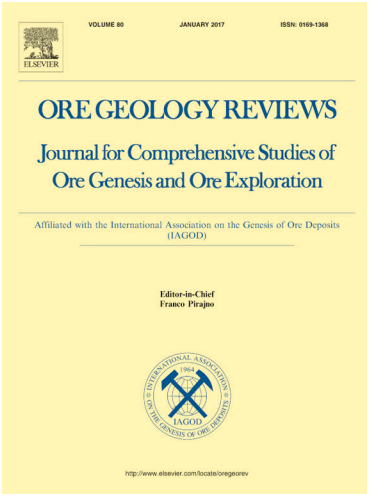

Timing and duration of Archean orogenic gold deposits in the Bourlamaque pluton, Val d'Or mining camp, Abitibi, Canada

Alain Tremblay, Gilles Ruffet, Jérémie Lemarchand

PII: S0169-1368(20)30709-5
DOI: https://doi.org/10.1016/j.oregeorev.2020.103812
Reference: OREGEO 103812

To appear in: *Ore Geology Reviews*

Received Date: 3 July 2020
Revised Date: 24 September 2020
Accepted Date: 28 September 2020

Please cite this article as: A. Tremblay, G. Ruffet, J. Lemarchand, Timing and duration of Archean orogenic gold deposits in the Bourlamaque pluton, Val d'Or mining camp, Abitibi, Canada, *Ore Geology Reviews* (2020), doi: https://doi.org/10.1016/j.oregeorev.2020.103812

Timing and duration of Archean orogenic gold deposits in the Bourlamaque pluton, Val d'Or mining camp, Abitibi, Canada.

TREMBLAY, Alain
Département des Sciences de la Terre et de l'Atmosphère, Université du Québec à Montréal, Canada
Tremblay.a@uqam.ca

RUFFET, Gilles
CNRS (CNRS/INSU) UMR 6118, Géosciences Rennes, F-35042 Rennes Cedex, France
Université de Rennes 1, Géosciences Rennes, F-35042 Rennes Cedex, France
Gilles.Ruffet@univ-rennes1.fr

LEMARCHAND, Jérémie[1]
Département des Sciences de la Terre et de l'Atmosphère, Université du Québec à Montréal, Canada
jeremie.lemarchand@gmail.com
[1]Present address; Département de biologie, chimie et géographie, Université du Québec à Rimouski, 300 Allée des Ursulines, Rimouski, Qc, G5L 3A1.

ABSTRACT

In the Val-d'Or mining district of the Archean Superior Province, the relationship between regional metamorphism/deformation and the timing of orogenic vein-type gold mineralization is debated; some authors arguing that gold mineralization was coeval with the regional D_2 deformation event and broadly synchronous with metamorphism, and others suggesting that it is 60 to 100 Ma younger than peak metamorphism. Using the $^{40}Ar/^{39}Ar$ method and the compilation of U-Pb or Pb-Pb ages of ore-related minerals, this contribution presents a geochronological study on the timing and the inferred duration of the formation of vein-type gold deposits hosted by the Bourlamaque pluton in the Val d'Or mining district. We present an extensive set (49 samples) of $^{40}Ar/^{39}Ar$ CO_2 laser probe data acquired on amphibole and white mica single grains from three major gold deposits, the Lac-Herbin, Beaufor and Beacon-2 mines. In each deposit, gold mineralization is host by shear and extensional quartz veins associated to steeply south-dipping networks of ductile shear zones. Barren north-dipping faults also occur at each deposit and are attributed to post-mineralization structural event(s). Amphiboles $^{40}Ar/^{39}Ar$ analyses yield magmatic crystallization ages clustering around 2704 Ma and

preserve evidences for at least two subsequent disturbances linked to probable hydrothermal circulation events at c. 2667 Ma and c. 2652 Ma. White micas $^{40}Ar/^{39}Ar$ age spectra from auriferous quartz veins and hosting mylonitic shear zones are typical of long-lasting and sequential dynamic recrystallization and suggest that Au-bearing hydrothermal circulation was establish, at least, around c. 2650 Ma, and followed by a succession of hydrothermal pulses at c. 2597, 2575, 2551, 2500 and 2452 Ma. $^{40}Ar/^{39}Ar$ ages distribution among the different deposits as well as between the auriferous quartz veins and hosting shear zones are consistent with fluids production and circulation along an active network of seismically active fault zones.

Keywords: Superior Province, Abitibi, orogenic gold, geochronology, duration.

1. Introduction

Orogenic gold deposits (Groves et al., 1998) are a widespread type of epigenetic ore deposits attributed to faulting and fracturing of the lithosphere and coeval hydrothermal fluid circulation at/or in the vicinity of compressional/transpressional plate boundaries. These gold deposits occur in accretionary terranes and collision zones of all geological periods but those hosted by Late Archean rocks worldwide contain a high percentage of the world gold resource (Goldfarb et al., 2001). Active crustal deformation is necessary to generate and maintain permeability and to sustain large-scale fluid flow in such hydrothermal systems (Cox, 2005), and isotopic geochronological data suggest that major deposits of a given mining district formed diachronically towards the end of c. 100 to 200 m.y. long evolutionary history of hosting rocks (e.g. Groves et al., 2000). In the Val d'Or mining district, most veins-type orogenic gold deposits, typified by the Sigma-Lamaque deposit (Daigneault, 1983; Robert and Brown, 1986; Dubé, 2018), have been interpreted either as shear zone-hosted (Sibson et al., 1988; Dubé, 2018) or fold-controlled (Cowan, 2020). In the Sibson's et al. (1988) fault-valve model of crustal-scale shearing, for instance, fluid pressure (P_f) build-ups below the seismogenic zone are linked with episodic seismic failures of the crust, the up-dip propagation of reverse fault-fractures and the drainage of mineralizing fluids along faults and related zones of fracture permeability, followed by post-failure mineral deposition and self-sealing (see also

Robert and Poulsen, 2001; Sibson, 2001; and Cox, 2001; 2005). That model has been, however, recently re-evaluated and disputed for the Sigma-Lamaque deposit (Cowan, 2020) but it still adequately accounts for gold-vein deposits hosted by isotropic batholithic intrusions such the Bourlamaque pluton (e.g. Tessier, 1990; Sauvé et al., 1993; Tremblay, 2001). In terms of P_f and strain rate (γ) (Fig. 1), the lifespan of such hydrothermal systems is believe to be concomitant with an unknown number of seismic failure events initiated along neo-formed and pre-existing reverse faults at the base, more or less, of the seismogenic zone, their functioning being synchronous with inter-seismic episodes of progressive P_f increases in excess of the lithostatic load ($P_f > \Phi_3$) lasting from decades to many thousands of years (Sibson et al., 1988; Sibson, 2001; Cox, 2001; 2005, among others).

In typical vein-type deposits, such as those of the Southern Abitibi Greenstone Belt of the Archean Superior Province of Canada (Fig. 2), the total reverse separation across the faults and shear zones hosting the gold mineralization is relatively low, in the order of a few hundred metres, although the vein systems can be of considerable vertical extent (>2 km). It has been suggested that this may represent an approximate total amount of c. 10^2-10^3 episodes of ~M7 seismic failures, if not more, for a single gold deposit along a given fault/shear zone system (Sibson et al., 1988; Cox, 2005). For comparison, the total fluid flux volume through mineralized faults of the Eastern Goldfield Province (Western Australia) suggests that it is the result of many hundreds or thousands of fault slip events (Sheldon and Ord, 2005). The determination of magnitude-frequency distributions for large earthquakes is a difficult task. It is highly imprecise, even in modern tectonic settings (e.g. Berryman et al. 2012; Scharer et al. 2014). Establishing the age of formation of gold mineralization and the time-period that corresponds to the development of a given series of fault-controlled auriferous veins is, however, of considerable importance for exploration and field-based strategies. In fossilized Archean hydrothermal systems that are accessible via surface exposure and underground mining, this can be studied by the isotopic dating of appropriate rock units and structures. Using the $^{40}Ar/^{39}Ar$ dating method and the compilation of U-Pb or Pb-Pb dating of ore-related minerals, this contribution presents an extensive geochronological

study on the timing and the inferred duration of the formation of typical vein-type gold deposits hosted by the Bourlamaque pluton in the Val d'Or mining district (Fig. 3) of the Abitibi Greenstone Belt.

2. Geological setting

The Abitibi Greenstone Belt (AGB) (Fig. 2) is made up of ultramafic, mafic, felsic volcanic rocks and syn-volcanic intrusions of Late Archean age. The volcanic domains are separated by narrow and linear belts of clastic sedimentary rocks that are associated with major fault zones forming lozenge-shaped patterns (Ludden and Hubert, 1986; Hubert, 1990; Percival, 2007). The youngest sequence of these clastic sedimentary rocks, the Temiskaming Group, was deposited above angular unconformities between ca. 2679 and ca. 2670 Ma (e.g. Robert et al., 2005). Both the volcanic and sedimentary rocks are intruded by a series of syn- and post-tectonic, dioritic to tonalitic plutons that span ages as young as ca. 2650 Ma (e.g. Robert, 2001). To the south, the AGB is in fault contact with the Pontiac subprovince along the Cadillac tectonic zone (CTZ, Fig. 2; Robert, 1989). The Pontiac subprovince (Figs. 2 and 3) contains rocks that are mainly younger than c. 2683 Ma (Mortensen and Card, 1993), and which consist of flyschoid wackes and pelites with minor volcanic rocks intruded by voluminous late tectonic granitoids (Fig. 2). Regional structures in both the Abitibi and Pontiac subprovinces are related to north-south compression during the Late Archean Kenoran orogeny (Percival, 2007). Regional metamorphism (~2660 Ma; Robert et al., 2005) is at subgreenschist to amphibolite facies in the AGB, whereas in the Pontiac subprovince, it increases from the biotite to the sillimanite zone within c. 2 km south of the CTZ (Dimroth et al., 1983; Powell et al., 1995).

In the Val-d'Or mining district (Fig. 3), rock units strike east-west and are tightly folded, almost subvertical and parallel to the trend of the regional structural fabric that is a weak to penetrative schistosity hosting downdip stretching lineations, and which has been ascribed to a D_2 event of regional deformation (Robert et al., 2005). The youngest volcanic rocks of the area, the Val d'Or and Héva formations (Fig. 3), yielded U-Pb zircon ages of 2704 ± 2 and 2702 ± 2 Ma, respectively (Scott et al., 2002). The

Bourlamaque pluton (2700 ± 1 Ma; Wong et al., 1991) is a calc-alkalic synvolcanic intrusion (Campiglio and Darling, 1976) which hosts several gold deposits (Fig. 3). Several generations of dikes, predating gold-bearing quartz vein mineralization, occur throughout the area and include aplite, pegmatite, and, more commonly, diorite dikes, the latter type has been interpreted as a stress guide for shear zone development in the Bourlamaque pluton (Belkabir et al., 1993). Syn- to late-tectonic intrusions range from diorite to tonalite and typically form small plutons that locally host gold-bearing quartz veins, such as in the Sigma-Lamaque deposit (e.g. Robert & Brown, 1986; Dubé, 2018). Post-tectonic intrusions consist of quartz-monzonite and granite. The Preissac-Lacorne batholith (Fig. 2) is a major syn- to late-orogenic intrusion of the Val d'Or mining district. It is made up of a composite series of intrusions in which two distinct types and ages of granitic rocks are present: an early, subalkaline to alkaline, monzodiorite-monzonite-granodiorite-syenite series emplaced between 2690 and 2670 Ma; and a younger, S-type garnet-muscovite granite series dated between 2660 and 2642 Ma, and probably derived from a major metasedimentary source (Feng et al. 1992; Ducharme et al., 1997; Daigneault et al, 2002). Finally, diabase dikes, presumably related to mafic dike swarms of the latest Archean-Early Paleoproterozoic (2.5-2.45 Ga) Matachewan Igneous Province (Ciborowski et al., 2015), record the youngest plutonic event of the area.

Robert (1990, 1994) distinguished two types of gold deposits in the Val d'Or mining district, (1) disseminated gold in massive, fractured, or brecciated wall rocks, and (2) vein-type orogenic deposits. Within the latter, quartz-carbonate-tourmaline veins are distinguished from quartz-carbonate-chlorite veins. The timing of the disseminated gold mineralization (type 1) is constrained by 2692 to 2696 Ma diorite dikes crosscutting the mineralization (Couture et al., 1994; Morasse, 1998). These deposits are therefore considered as "early". By analogy, quartz-carbonate-chlorite veins of type 2 gold deposits are typically crosscut by mafic dikes, overprinted by deformation, and were also classified as "old" (Robert, 1994). The auriferous quartz-carbonate-tourmaline veins (i.e. the quartz-carbonate veins of Robert et al., 2005), classified as "young" by Robert (1994), were formed after the peak of metamorphism and are almost undeformed. They

158 are hosted by shear zones and quartz-carbonate ± tourmaline ± scheelite vein systems,
159 and were typified in the Sigma-Lamaque and the Perron-Beaufor deposits (Fig. 3).
160 Although that it has been recently contested by Cowan (2020), the formation of gold-
161 hosting shear zones is usually considered as broadly coeval with faulting along the CTZ
162 (Figs. 2 and 3; Sibson et al., 1988; Bedeaux et al., 2017; Dubé, 2018), that is interpreted
163 as a 1st-order structure to which 2nd- and 3rd-order structures are subordinate, the latter
164 hosting most gold-bearing quartz-carbonate-tourmaline veins deposits of the Val-d'Or
165 district (Robert, 1990; Neumayr et al., 1999). Hydrothermal alteration aureoles related to
166 these shear zones and veins crosscut regional metamorphic isograds and destabilize the
167 igneous and/or metamorphic minerals paragenesis of hosting rocks, attesting to a late- to
168 post-metamorphic origin. The maximum age of the younger gold-rich hydrothermal event
169 is constrained to <2680 Ma, based on U-Pb zircon ages from magmatic rocks hosting the
170 mineralization at the Sigma-Lamaque deposit (see Neumayr et al., 1999). According to
171 Robert et al. (2005), quartz-carbonate-tourmaline vein deposits postdated sedimentation
172 of the Temiskaming Group and formed synchronously with regional metamorphism and
173 late D_2 shortening at c. 2670-2660 Ma.
174
175 **3. Structural characteristics of the studied deposits**
176 For this study, we have mapped (or re-mapped) sections of the Lac-Herbin (Figs.
177 4 and 5a), Beaufor and Beacon-2 mines (Figs. 5b and 5c). The Lac-Herbin and Beaufor
178 mines (Lemarchand, 2012; Tessier, 1990; Tremblay, 2001) consist of 8 and 20
179 underground levels, respectively, over a vertical distance of c. 400 and 650 metres,
180 whereas the Beacon-2 deposit (Williamson, 2001) is a 2-level mine that is now used for
181 educational underground mining and security purposes.
182 In each deposit (Figs. 4 and 5), moderately-to-steeply (40°–70°) south-dipping,
183 East-West trending brittle-ductile reverse shear/fault zones filled with more-or-less
184 continuous quartz-carbonate-tourmaline veins and associated subhorizontal
185 extensional/sigmoidal flat veins host gold ore zones. All gold-hosting fractures were
186 filled while the shear zones were still active and with the same veining material. Gold is
187 associated with sulphides (mostly pyrite) and occurs within 1- to 2-metres-wide, sheared

and extensional quartz-tourmaline-sulphides-carbonate veins. Wallrocks are mylonitized granitic rocks hosting downdip stretching lineations and slickenside striae. The contact with the adjacent undeformed to slightly deformed plutonic rocks is marked by a gradual decrease in the intensity of mylonitization over a distance of 50 cm or less, and fault rocks vary accordingly from protomylonites to mylonites and ultramylonites from the margins toward the center of the shear zones. The rotation of the schistosity, and the presence of C-S fabrics, discontinuous shear bands, and folded extensional veins indicate a reverse sense of shearing. Mylonites and ultramylonites are fine grained, i.e., grains less than 0,1 mm in diameter. Feldspar porphyroclasts are present and occur within a matrix of ribonned chlorite-muscovite (sericite)-quartz-carbonate. Crystal-plastic textures in quartz grains and brittle fracturing of feldspars attest to brittle-ductile conditions of deformation at greenschist-grade conditions (350°–400°C; Passchier and Trouw, 1996). The mineralogy of the gold-bearing veins is typical of the greenschist facies (≤ 450°C). Beaudoin and Pitre (2005) proposed an average regional temperatures of 350°C during the formation of orogenic gold-veins in the Val d'Or mining district. This is in agreement with a minimum temperature estimate of 250-300°C for gold-bearing quartz veins at Lac-Herbin mine as suggested by Rezeau et al. (2017) who identified three unrelated fluid inclusion types, the oldest ones being related to the main filling stage of gold veins. These data are also consistent with temperature of 300-400 °C and 260-380°C reported by Robert and Kelly (1987) and Kerrich and King (1993), respectively, and with temperatures varying between 300°C and 450°C suggested for the Cadillac tectonic zone (Neumayr and Hagemann, 2002).

The structural analysis suggests that, at each mine site, the mineralized zones represent two or three gold-rich zones that were originally more or less continuous and dissected by a series of north-dipping, oblique-reverse dextral faults which lack evidence for pervasive hydrothermal alteration (Fig. 5; Tremblay, 2001; Lemarchand, 2012; Williamson, 2001). These barren, east-west-trending brittle faults which crosscut each deposit, are the Lac-Herbin-Sud fault at Lac-Herbin mine (Fig. 5a), the Perron and Beaufor faults at Beaufor mine (Fig. 5b), and the Beacon and New-Vein faults at Beacon-2 mine (Fig. 5c). Figures 5b and c shows that in the Beaufor and Beacon-2 mines, these

faults divide the deposits into a series of structural blocks between which it is difficult to correlate the auriferous zones. The width of the faults varies from 5 to 10 metres. They are marked by chlorite schist enclosing brecciated wall rock and barren quartz-chlorite veins. The chlorite schist is cut by discontinuous fractures filled by gouge material and/or cataclastic breccia. The large range of grain size in cataclasites, the limited recrystallization of quartz grains, and the predominance of intragranular fracturing and pressure solution attest to very low-grade conditions of deformation (≪ 300°C).

4. $^{40}Ar/^{39}Ar$ geochronology

The establishment of unequivocal «absolute» ages for vein-type gold deposits is a subject of debate (e.g. Goldfarb et al., 2001; Robert et al., 2005). Among the isotopic dating methods (U-Pb, Sm-Nd, ^{39}Ar-^{40}Ar) used to estimate the timing of orogenic gold in Archean terranes, a number of authors believe that the $^{40}Ar/^{39}Ar$ method is less robust and yields ages that are often much younger than could seemingly be inferred by geologic facts. They consider such age results as minimum estimates (e.g. Kerrich and Cassidy, 1994; Powell et al., 1995; Groves et al., 2000; Robert et al., 2005). We disagree with that statement and, in the following section, it will be argued that with the appropriate analytical approach and data representations, the $^{40}Ar/^{39}Ar$ method yields age results that are consistent with a long-lasting incremental evolution of vein-type deposits. It is emphasized here, however, that a large number of $^{40}Ar/^{39}Ar$ analyses is the best way to address the thermo-chronological evolution of complex natural systems such as vein-type orogenic deposits, which are characterized by a protracted and multistage structural and hydrothermal evolution during which the oldest radiogenic components are progressively obliterated by younger events, making their recognition difficult, sometimes impossible.

For this study, three types of rocks have been targeted for amphibole and mica single-grain $^{40}Ar/^{39}Ar$ dating, (i) undeformed dioritic intrusions, (ii) mylonites derived from plutonic rocks hosting auriferous quartz-carbonate-tourmaline veins, and (iii) quartz-carbonate-tourmaline veins. 49 samples (55 analyses counting c. 1320 heating steps and c. 390 blanks for c. 700h of data acquisition) have been analyzed, most of them from the Lac-Herbin deposit (Lemarchand, 2012). To our knowledge, this is the most

extensive $^{40}Ar/^{39}Ar$ geochronological study performed on a single orogenic gold deposit. Seven samples of amphibole come from the undeformed diorite at Lac-Herbin; 5 from underground workings and two from surface exposures (Fig. 6). Among the 42 samples of white mica, 26 are from the Lac-Herbin mine (Figs. 7 to 12), 7 from surface exposures of the Bourlamaque pluton in the vicinity of the Lac Herbin mine (Fig. 13), 6 from the Beaufor mine (Fig. 15) and 4 from the Beacon-2 mine (Fig.16). The overall distribution of white mica samples between quartz-carbonate-tourmaline veins and hosting shear zones is 60% and 40%, respectively. Whenever possible, the sampling of white mica pairs from quartz-carbonate-tourmaline veins and hosting mylonitic rocks has been favoured.

4.1 $^{40}Ar/^{39}Ar$ analytical method, data processing and presentation

Samples were irradiated in two batches, IR14 and IR16, at McMaster Nuclear Reactor (Hamilton, Ontario, Canada) in its 5C high neutron flux facility. They respectively lasted 134.36h and 133.42 h with global efficiencies (J/h) of 3.594×10^{-4} h^{-1} and 3.999×10^{-4} h^{-1}. Single grains of amphiboles and white micas (entire crystals or fragments) were analyzed by the $^{40}Ar/^{39}Ar$ method in step-heating using a CO_2 laser probe coupled with a MAP 215 mass spectrometer. The analytical procedure is described by Ruffet et al. (1991, 1995, 1997). The irradiation standard was amphibole Hb3gr (Turner et al. (1971); Roddick (1983); Jourdan et al. (2006) and Jourdan & Renne (2007) – 1081.0 ± 1.2 Ma according to Renne et al. (2010) and Renne et al. (2011)). Blanks were performed routinely each first or third/fourth run, and subtracted from the subsequent sample gas fractions. Errors of apparent ages (ages of individual heating steps in age spectra which can be broken down into low, intermediate and high temperature apparent ages) are plotted at the 1σ level and do not include the errors on the $^{40}Ar^*/^{39}Ar_K$ ratio and age of the monitor and decay constant. Plateau ages were calculated if 70% or more of the $^{39}Ar_K$ was released in at least three or more contiguous steps which define apparent ages agreeing, to within 2σ, with the integrated age of the plateau segment. This 70% threshold, a requirement criterion that we use in all our geochronological studies, is much more restrictive than the 50% threshold set subjectively, in their own words, by Fleck et

al. (1977) and still adopted by most of the users of the $^{40}Ar/^{39}Ar$ method. As the amount of $^{39}Ar_K$ released is not a disqualifying criterion, we have for a long time associated to our restrictive age plateau concept used for "simple" mineral phases, the concept of pseudo-plateau (Cheilletz et al., 1999), which meets the same statistical criteria except for the cut-off threshold (<70% of $^{39}Ar_K$), and which is much more efficient for the analysis of complex mineral phases. The errors on the $^{40}Ar^*/^{39}Ar_K$ ratio and age of the monitor and decay constant are included in the final calculation of the error margins on the pseudo- and plateau ages. $^{40}Ar/^{39}Ar$ ages are provided with 1σ errors. Analytical data and parameters used for calculations (e.g. isotopic ratios measured on pure K, Ca and Cl salts; mass discrimination; atmospheric argon ratios; J parameter; decay constants) and reference sources are available in the supplementary data repository.

Due to complexity of ^{39}Ar-^{40}Ar results of this study, especially for white micas, their processing must go beyond the simple visual examination of age spectra. De Putter et al. (2015) and De Putter and Ruffet (2020) presented and developed tools for the visualization and processing of complex $^{40}Ar/^{39}Ar$ systems governed by fluid inflows. Three of these tools are classical: the plateau (Fleck et al., 1977) and pseudo-plateau age (PPA) (Cheilletz *et al*., 1999) concepts, and the probability density diagrams, which have been first used for ^{39}Ar-^{40}Ar data by Deino & Potts (1992). Others tools are more atypical; (i) the degassing and the weighted age spectra, which were designed to visualize Ar degassing kinetics of $^{40}Ar/^{39}Ar$ experiments, and (ii) the resizing of age spectra which was developed to ensure their statistical representativeness. Because of their prominent roles in this study, the two latter tools are described below.

4.1.1 Degassing and weighted age spectra. For $^{40}Ar/^{39}Ar$ analyses of multi-component systems, the kinetics of argon degassing can be visualized by means of a degassing spectrum. The degassing spectrum reports for each step, vs. $\%^{39}Ar_K$, the amount of ^{A}Ar (with mass number A=36 to 40) weighted by the temperature difference with the previous step (ΔT°), this ratio being normalized between 0 and 1. It is expressed as $(^{A}Ar/\Delta T°)/(^{A}Ar/\Delta T°)_{Max}$ versus $\%^{39}Ar_K$ (with $^{A}Ar = {}^{40}Ar^*, {}^{39}Ar_K, {}^{37}Ar_{Ca}, {}^{36}Ar_{Atm}$). A degassing spectrum allows the visualization of variations in the degassing rate, thus

providing information on the isotopic/radiogenic components that may be present in the analyzed material as well as on transitions between them during degassing. A conventional age spectrum is a raw representation of the $^{40}Ar/^{39}Ar$ experiment and does not reflect variations in the degassing rate during the successive temperature increments. Different steps corresponding to the same amount (Q) of $^{39}Ar_K$ released will have the same width on such spectra, regardless of the temperature increments ($\Delta T°$) that produced them. The weighting of $^{39}Ar_K$ degassing by temperature increments, expressed by $\%((^{39}Ar_K/\Delta T°) / (^{39}Ar_K/\Delta T°)_{Max})$, yields a weighted age spectrum that integrates the degassing rate and which is the result of the combination of the degassing spectrum and the conventional age spectrum. On such spectra, the width of a step accounting for an amount Q of argon released during a temperature increment $\Delta T°$ will be the same as that of a step accounting for an amount x.Q of argon released during a temperature increment $x.\Delta T°$. Hence, a weighted age spectrum allows depicting weakly expressed but clearly identified radiogenic components (associated with degassing peaks) in proportion to their degassing rates. Insofar as temperature (T°) measurement during CO_2 laser probe analysis is a major difficulty, the laser power control voltage ($V_{T°}$), a proxy indicator, is substituted for it. Therefore, the degassing spectrum $((^{A}Ar/\Delta V_{T°})/(^{A}Ar/\Delta V_{T°})_{Max}$ versus $\%^{39}Ar_K$) and weighted age spectrum $(\%((^{39}Ar_K/\Delta V_{T°})/(^{39}Ar_K/\Delta V_{T°})_{Max})$ would be used only in order to identify radiogenic components in the analyzed materials and relate them to the observed age spectra shapes, which implies that weighted age spectra should not be directly used to calculate plateau or pseudo-plateau ages.

4.1.2 The resizing of age spectra (Resized age spectra). The use of probability density diagrams involves ensuring that the age spectra that are compiled to construct them are equally statistically representative. In such diagrams, all the heating steps contribute almost equally since they are weighted by their respective errors but not by their respective amount of degassed $^{39}Ar_K$. $^{40}Ar/^{39}Ar$ experiments are never perfectly identical (i.e. in terms of number of steps and % of $^{39}Ar_K$ degassing per step) because the degassing control is not perfect and analyzed samples are inevitably dissimilar. Resizing the compiled age spectra is used to standardize their statistical representativeness in

probability density diagrams, thus ensuring that all age spectra have the same number of steps and that each step represents the same amount of $^{39}Ar_K$ degassed. Such resizing of apparent ages obviously requires a reappraisal of their respective errors by respecting the principle of weighted averages.

Finally, it is important to prioritize the panel of tools presented above. Degassing spectra and weighted age spectra are basically a support to the interpretation of analyses, allowing data to be visualized in a different and more complete way. Conventional age spectra are at the heart of the validation process. They alone allow the statistical validation of significant ages through plateau and pseudo-plateau calculations which attest to the concordance of the apparent ages within a segment of the age spectrum and therefore to the isotopic coherence of the argon degassing for this domain, signaling the occurrence of a coherent radiogenic component. Probability density diagrams, either conventional or calculated after resizing the age spectra, are intrinsic validation tools since they represent the probability of occurrence of apparent ages for a given age range. They are also a synthetic representation of the validated ages.

4.2 Isotopic closures - from cooling to (neo/re)crystallization

A radiochronological system is the combination of the crystal lattice of a mineral phase and an isotopic pair consisting of a radiogenic element and its radioactive precursor, e.g. $^{40}Ar^*$ and ^{40}K, the latter (K) being or not being a constituent of the lattice. The analysis of isotopic systems, particularly those involving noble gases, has long focused on the behaviour of the radiogenic element, in this case $^{40}Ar^*$, the host minerals being themselves considered inert and the fate of the isotopic system being exclusively governed by the diffusion of the gas under temperature control, as described by Fick's laws. This led to the notion of isotopic blocking temperature initially introduced by Jäger et al. (1967), formalized as the isotopic closure temperature (Tc) by Dodson (1973) and then nuanced with the notion of isotopic closure window by Dunlap (1997). Therefore, during cooling and for a given isotopic system (mineral and isotopic pair), the isotopic chronometer initializes when diffusion becomes negligible because the temperature has dropped below its isotopic closure temperature.

Tc for amphibole is difficult to estimate. In addition to the effect of cooling rate and size of diffusion domains, amphibole diffusivity is also influenced by ionic porosity (Fortier and Giletti, 1989; Dahl, 1996). On the basis of natural hornblende compositions measured by various authors (i.e. Colville et al., 1966; Leake, 1978; Robinson et al., 1982), Dahl (1996) suggested a Tc range of 480-550°C, re-evaluated at 550-650°C by Villa (1998) using experiments of Kamber et al. (1995) suggesting that, depending on the crystal lattice characteristics, hornblende may form a closed system to Ar diffusion for temperatures as high as 580°C for cooling rates of 0.7°K/Ma (Villa et al., 1996).

Using experimental muscovite diffusion coefficients yielded by Harrison et al. (2009) and calculations performed by Pitra et al. (2010) with various effective diffusion radii (100 to 1000 μm) and cooling rates (1 to 1000°C/Ma), a 390-590°C temperature range could be estimated for white micas. White micas analyzed in this study are frequently sericite or poly-crystalline white mica (muscovite?) aggregates and it would be thus reasonable to consider lower isotopic closure temperatures, although it is difficult to quantify due to smaller effective diffusion radii than in well-crystallized muscovite crystals.

As shown by Cheilletz et al. (1999) and Alexandrov et al. (2002), in a context where deformation and/or fluid circulation are important parameters, the constituent mineral of the isotopic system is a weak link as it can evolve through partial or total static or dynamic recrystallization (*sensu lato*, i.e. in the broad sense of a process altering the crystal lattice) with a sequential reset of the ^{40}K-^{40}Ar couple at the scale of internal recrystallized zones. This process can lead to the coexistence of intra-crystalline domains with different chemical and isotopic compositions and thus distinct ages. Dunlap (1997) suggested that white micas from mylonites record neocrystallization related to ductile deformation at c. 350-250°C rather than cooling. The role played by hydrothermal fluids in the ^{40}K-^{40}Ar isotopic system is so significant that Villa (2010) stated, quote «*Mineral geochronometers should be viewed as «geohygrometers» that essentially date the fluid circulation episodes*». Tartese et al. (2011) exemplified this concept by evidencing sequential fluid-assisted resets of muscovite K-Ar isotopic chronometer during a time

span of 16 Ma after emplacement at shallow depth (3-6 km; Tartèse and Boulvais, 2010) of a syn-kinematic leucogranite.

As amphiboles are part of the primary mineral paragenesis, they might potentially date emplacement/crystallization of the Bourlamaque pluton, a small granitic body (23 x 12 km), which foresees rapid cooling. Subsequent disturbing events, which may induce partial or total recrystallization of these primary amphiboles, arise after the pluton has cooled, below the amphibole isotopic closure temperature. White micas are part of a metamorphic minerals paragenesis and hydrothermal alteration which developed at greenschist facies conditions (see sections 2 and 3), below or at closing temperatures, and may record crystallization as old as the early stages of growth. Subsequent alteration(s) of the earliest white micas, detected by disturbed $^{40}Ar/^{39}Ar$ age spectra with characteristic shapes (staircase, saddle; e.g. West and Lux, 1993; Dunlap, 1997; Cheilletz et al., 1999; Alexandrov et al., 2002; see section 5.2.1) would have occurred below isotopic closure temperature. The processing of these disturbed age spectra allows to estimate the age of partial/total recrystallization(s) which affected pre-existing minerals or to date the newly crystallized sub-grains (neocrystallization) aggregated with pre-existing ones.

5. RESULTS

5.1 Amphiboles

Typical $^{40}Ar/^{39}Ar$ amphibole age spectra for undeformed diorite samples are shown in Figure 6. With the exception of sample TG-AMPH, all amphibole analyses were duplicated. JS-1 (a common diorite facies) and TG-AMPH (a differentiated diorite facies) were sampled at surface in the Lac-Herbin mine area, while the other five samples were taken at levels 15, 20, 25, 29 and 30 of the Lac-Herbin mine.

All amphibole age spectra from the surface down to level 20 are disturbed with either a staircase shape (e.g. J15-2α; Fig. 6e) or a saddle shape (e.g. JS-1α and β; Fig. 6c). These disturbances in age spectra generally correlate with a decrease of $^{37}Ar_{Ca}/^{39}Ar_K$ ratios ($^{37}Ar_{Ca}/^{39}Ar_K = CaO/K_2O / 2.179$; Deckart et al., 1997) which reflect the chemical alteration of amphiboles, probably in relation to partial recrystallization. In spite of this, these amphiboles provide the oldest pseudo-plateau ages of this study, either in the high

temperature steps (e.g. J20-6α and β; Fig. 6f), or on sidewalls of saddles (e.g. JS-1α and β; Fig. 6c). These $^{40}Ar/^{39}Ar$ results allow the calculation of a mean age of 2704.4 ± 2.2 Ma (Figs. 6a and b), which is in good agreement with the zircon U-Pb age obtained by Wong et al. (1991) (2699.8 ± 1.0 Ma) for the Bourlamaque pluton. This coincidence of K-Ar and U-Pb ages as well as the above-mentioned isotopic closure temperatures of amphiboles suggest that the $^{40}Ar/^{39}Ar$ age of c. 2700 Ma approximates the crystallization of amphiboles (Fig. 6b).

In contrast, amphiboles from the lowermost levels (25 to 30; Figs. 6g, h and i) yield less disturbed age spectra, which allow the calculation of plateau ages in the range 2665-2668.5 Ma, with no evidence of the initial c. 2700 Ma crystallization stage. These amphiboles are characterized by $^{37}Ar_{Ca}/^{39}Ar_K$ ratios in the order of 9.8-11.9, lower than those yielded by amphiboles of the uppermost levels (i.e. which yield $^{37}Ar_{Ca}/^{39}Ar_K$ ratios of 13.7 to 17.1). These variations in ages and chemical composition (Ca/K ratios) as a function of depth (Fig. 6j), suggest that amphiboles from deeper domains were recrystallized during an event, labelled "event #1" on Figure 6b, which led to a total reset of their K-Ar isotopic system. This same event also explains partial recrystallizations expressed by staircase or saddle-shaped age spectra provided by some amphiboles collected at the surface (JS-1α and TG-AMPH; Figs. 6c and d). A mean age of 2666.9 ± 1.8 Ma can be calculated for that event #1 (Figs. 6a and b). Most amphibole age spectra from levels 25 to 30 (Figs. 6g, h and i) also show a coherent disturbance in their low to intermediate temperature steps, at the expense of intermediate to high temperature ones which characterize event #1, with a corresponding pseudo-plateau ages bracket allowing the calculation of a mean age of 2651.8 ± 3.6 Ma, labelled event #2 (Figs. 6a and b). This same perturbation could be also related to the saddle-shaped disturbance observed on amphibole age spectra of level 20 (Fig. 6f). Finally, saddle-shape spectra observed on two amphiboles from the surface (JS-1β; Fig. 6c) and at level 25 (JSN25-4α; Fig. 6g) suggest the occurrence of a third, more discrete, disturbing event at 2634.4 ± 3.6 Ma, labelled event #3 on Figure 6a.

Amphibole data are synthesized on Figure 6a and b, which emphasizes the timing of the three recrystallization events. Events #1 and #2 are primarily observed at the lower

levels of the Lac-Herbin mine. Recrystallizations deduced from the processing of $^{40}Ar/^{39}Ar$ analyses related to these events suggest that fluids, in disequilibrium with amphiboles, percolated at temperatures below their isotopic closure temperature. Our interpretation is that the crystallization of amphiboles occurred at ca. 2700 Ma, whereas the ca. 2666 Ma ages record a recrystallization event related to metamorphism. We admit, however, that events #1 and #2, at c. 2667 and c. 2652 Ma, possibly belong to a single geological event, which is regional metamorphism and syn- to late-orogenic plutonism related to the Preissac-Lacorne batholith. Event #3 can be related to the emplacement of the youngest phases of that same batholite, i.e. the ~2645 Ma Lamotte and Lacorne monzogranite plutons (Ducharme et al., 1997).

5.2 White micas

Scarce white micas found in sheared quartz veins are mostly sericite whereas those disseminated in the hosting shear zones are, with rare exceptions, poorly crystallized. Muscovite (*s.s.*) has only exceptionally been observed. Figures 7 to 14 show white mica age results obtained from the Lac-Herbin mine and surrounding surface area, whereas those for the Beaufor and Beacon-2 mines are shown in Figures 15 and 16, respectively.

The Lac-Herbin mine (Figs. 7 to 14) represents the vast majority of the white mica samples that were analyzed. It was sampled from levels 15 to 32 (150 to 370m depth), and seven surface samples were collected in the area surrounding the mine. The $^{40}Ar/^{39}Ar$ analyses were processed by grouping them by structures as follows, HW (Fig. 7), S2 (Fig. 8), S1 (Fig. 9), S3 (Fig. 10), WE (Fig. 11), HW3 + Bonanza + Flat (Fig. 12). The analyses of the surface samples are shown in Figure 13 and all the results from the Lac Herbin area are synthetized in Figure 14. At the Beaufor mine (Fig. 15), samples were collected in zones C and F of level 1750 (533m depth) and in the vicinity of Dike 01 fault zone (see Tremblay, 2001) whereas at the Beacon-2 mine (Fig. 16), the Canmet (Discovery) and New Vein structures were sampled on level 70 (70m depth). In the following, the names of samples taken at the Beaufor and the Beacon-2 mines begin with BF1750 and BC, respectively.

Among a total of forty-six $^{40}Ar/^{39}Ar$ experiments carried out on white micas, only two (J15-2-WEa (Fig. 11) and BF1750-5a (Fig. 15)) allowed the calculation of plateau ages (≥ 70% of $^{39}Ar_K$ degassed). The remaining experiments produced multi-stepped age spectra with frequent staircase shape interspersed with one or more flat segments (e.g. J25-HW-QTZ-09; Fig. 7), more rarely, saddle shapes (e.g. J25-HW-MYL-09; Fig. 7), or a combination of both types of spectrum (e.g. BF 1750-7C; Fig. 15). As mentioned in section 4.1, the shape of age spectra expresses the partial re-crystallization of pre-existing grains or the aggregation of new (neo-formed) sub-grains that occurred after initial crystallization, below isotopic closure temperature, saddle shapes being associated with partial recrystallization whereas composite/aggregated mica grains usually produce stepped age spectra. The interpretation of these disturbed age spectra is intended to deconvolve the measured signal that expresses the coexistence and intermingling of multiple radiogenic components as illustrated hereafter through some characteristic examples. Six different radiogenic components, whose age decreases from c. 2650 Ma to c. 2450 Ma, have been identified and labelled as α, β, χ, δ, ε and φ. They are illustrated hereafter through examples of characteristic age spectra found for white micas.

5.2.1 Interpretative approach of $^{40}Ar/^{39}Ar$ age spectra. The following section aims at presenting the interpretative approach of disturbed age spectra yielded by most of our white micas $^{40}Ar/^{39}Ar$ experiments through a few examples.

A saddle-shaped age spectrum obtained by $^{40}Ar/^{39}Ar$ analysis of a single grain of white mica expresses the interaction between two radiogenic components whose coexistence results from partial recrystallization of a pre-existing material during a subsequent hydrothermal event (Cheilletz et al., 1999; Alexandrov et al., 2002; Castonguay et al., 2007; Tartèse et al., 2011; Tremblay et al., 2011). According to the interpretation proposed by Alexandrov et al. (2002), the apparent ages of the saddle edges in the low and high temperature steps provide a minimum estimate of the age of the pre-existing material whereas the apparent ages that define the base of the saddle provide a maximum estimate of the age of the event that induced partial recrystallization. Following this interpretative model, pre-existing radiogenic component of white mica

J25-HW-MYL-09 (Fig. 7), from a shear zone hosting the HW quartz vein at the Lac Herbin mine, would be as old as c. 2575 Ma. This "former" component will be referred to as χ. Then, the mica grain has been partially recrystallized at the earliest around c. 2545 Ma, which is also the age of a new radiogenic component, which will be referred to as δ.

Most of our white mica analyses provided multi-stepped age spectra that express aggregations, via dissolution/recrystallization/neocrystallisation processes, of increasingly younger sub-grains as fluid inflows (hydrothermal pulses) occur. $^{40}Ar/^{39}Ar$ analyses of composite white micas thus produce complex degassing spectra with several degassing peaks (increased degassing rates), which may partially overlap, expressing more or less individualized and distinct radiogenic components. Furthermore, despite very detailed stepwise heating experiments, some sub-components of the analyzed grains are sometimes weakly expressed via classical representations (usual age spectrum) simply because they represent only a small proportion of the analyzed material. For these complex age spectra, the analysis of the argon degassing kinetics and the implementation of the weighting process (see section 4.1) allows to refine their interpretation. Hence, white mica J25-HW-QTZ-09 from a quartz vein hosted by the HW structure, yielded a typical multi-stepped age spectrum which shows two flat segments in the low and in the high temperature steps, but also a more discrete one in the intermediate temperature domain (Fig. 7). With the exception of the very low temperature steps (first 10% of $^{39}Ar_K$ released), the degassing spectrum shows three domains/peaks (ε, δ, χ), separated from each other by a drop in the degassing rate (Fig. 7), which characterize the degassing cycle of three distinctive sub-grains or isotopic components (ε, δ and χ) within the composite mineral system represented by this sample. The degassing peaks/cycles ε and χ coincide perfectly with the two flat segments defined by the low and high temperature steps of the age spectrum. It is therefore reasonable to assign ages of 2503.5 ± 2.2 Ma and 2574.4 ± 3.7 Ma, respectively, to these radiogenic components on the basis of pseudo-plateau ages that can be calculated from the corresponding flat segments of the age spectrum. The main degassing peak (δ) in the intermediate temperature domain is more complex. Apparent ages of the corresponding segment within the age spectrum increase steadily from c. 2505.5 Ma, matching perfectly the age of the low temperature component ε, to a

flat segment for which a pseudo plateau age of 2543.9 ± 4.0 Ma can be calculated (Fig. 7). Assuming that this degassing peak is related to a component δ with an age of c. 2544 Ma, we may consider that it has been affected by partial recrystallization/dissolution during the growth of the younger ε component. Nevertheless, it cannot be excluded that the onset of degassing peak δ incorporates the tail of the low temperature degassing peak ε due to incomplete separation or partial overlapping between ε and δ. Under this assumption, the apparent age progression would simply reflect the transition from one component to the other (ε → δ).

Weighting the age spectrum of sample J25-HW-QTZ-09 (Fig. 7) by integrating the degassing rate doubles the width of the flat segment at c. 2544 related to component δ. The weighted age spectrum thus shows that, despite the moderate contribution to the overall $^{39}Ar_K$ released, the signal produced by component δ is of major importance in the shaping of the age spectrum. Similar mechanisms likely govern the transition between components δ and χ revealed by high-temperature steps, which is also associated with a small degassing peak (Fig. 7). The pseudo-plateau age calculated from the related flat segment of the spectrum suggests that component χ could be as old as 2574.4 ± 3.7 Ma. If, during transitions between components (e.g. ε→δ or δ→χ), the above-mentioned partial recrystallizations/dissolutions remain limited, then the process of sub-grain aggregation (stepped age spectrum), allows a better preservation and identification of the oldest phases than after a pervasive partial recrystallization (saddle-shaped age spectrum), and the different radiogenic components are more easily separable during stepwise heating experiments.

Aggregations are sometimes less complex with coexistence of only two components as for white mica JSN17-4-HWb (Fig. 7). Its stepped age spectrum with flat segments in low to medium and in high temperature domains, associated with two distinct degassing peaks, results from the successive degassing of two radiogenic/mineral components. The weighting process highlights a first degassing sequence, related to a component labelled χ, as old as 2572.7±4.3 Ma, because of its age concordance with the previously identified high temperature component of white mica J25-HW-QTZ-09. It is

followed by a second degassing sequence in high temperature domain which expresses the transition towards an older component, labelled β, as old as 2602.5 ± 7.8 Ma.

A small proportion of the $^{40}Ar/^{39}Ar$ age spectra combine stepped and saddle shapes. This is the case for our fourth example provided by white mica BF1750-7C (Fig. 15) from a sheared quartz vein of zone C of the Beaufor mine. This analysis yielded an overall saddle shaped spectrum. However, in the low temperature steps (<10% of $^{39}Ar_K$ released), it shows two small flat segments associated with degassing peaks attributed to sub-grains degassing. One of these peaks (labelled β), between 5 and 10% of the $^{39}Ar_K$ released, is particularly well-expressed. The weighting process for this analysis amplifies that flat segment by a factor of 3, and a pseudo-plateau age at 2600.8 ± 6.8 Ma can be calculated. The degassing of component β is preceded by that of component χ, which is characterized by a small peak associated with a small flat segment in the age spectrum (between 2.5 and 5% of $^{39}Ar_K$ released), allowing the calculation of a pseudo-plateau age at c. 2573 Ma (Fig. 15). This latter component χ is substantial as it is also responsible for and constitutive of the saddle shape that characterizes most of the age spectrum. As previously explained, component χ grows during hydrothermally-induced partial recrystallization of a pre-existing component, labelled α, preserved in high temperature degassing domain of white mica BF1750-7C (Fig. 15) and at least as old as c. 2650 Ma. The latter component, α, is also preserved in the high temperature steps of age spectrum yielded by white mica NW-DUM-5B (Fig. 13), which was collected from a surface shear vein in the vicinity of the Lac-Herbin mine. Sample NW-DUM-5B seems to be an aggregate/composite grain preserving, in addition to component α, evidences for components β and δ (Fig. 13), with component β partially recrystallized during an hydrothermal event that induced growth of younger component δ (Fig. 13).

Both previous experiments show that younger components that grow at the expense of older ones during hydrothermally-induced partial recrystallizations (χ at the expense of α for BF1750-7C and δ at the expense of β for NW-DUM-5B), form concomitantly as sub-grains aggregate with pre-existing ones. This suggests that partial recrystallization of pre-existing phases, growth of new components at the expense of pre-existing one and neocrystallization of new subgrains proceed concurrently through

606 dissolution-precipitation processes. Such an hypothesis explains why component α,
607 which is the oldest that has been detected on white micas, is only exceptionally
608 preserved, simply because the sequential and incremental hydrothermal evolution of the
609 system gradually erases the oldest components, a process very similar to what has been
610 described by De Putter and Ruffet (2020) for a $^{40}Ar/^{39}Ar$ study of Mn oxides developing
611 during the propagation of oxidation fronts in weathering profiles.
612
613 *5.2.2 Data synthesis.* All the identified components (α, β, χ, δ, ε and φ) were not
614 simultaneously detected within a single white mica grain. Their presence in the analyzed
615 white micas can be discontinuous, either because a given component is not detected or
616 absent in a given experiment. However, three different components were frequently
617 observed, exceptionally four. In fact, all experiments contain several radiogenic
618 components, including the two analyses that allowed the calculation of plateau ages, both
619 attributed to component δ, i.e. white micas J15-2-WEa at 2549.0 ± 3.9 Ma (a sheared
620 wall rock of the WE zone of the Lac Herbin mine; Fig. 11) and BF1750-5a at 2560.7 ±
621 3.3 Ma (a quartz vein from zone E of the Beaufor mine; Fig. 15) which preserve former
622 high temperature components χ and β, respectively.
623 Among all these components, α is the less well-preserved (see section 5.2.1). It
624 has been, however, identified in two samples, NW-DUM-5B (Fig. 13) and BF1750-7C
625 (Fig. 15), and could be as old as c. 2650 Ma.
626 Component β is well-represented among the analyses. It is the second oldest
627 component with a mean age of c. 2597 Ma, and frequently appears as a high-temperature
628 residual component in several age spectra. Component β is usually reworked by one or
629 more younger age components, for instance; χ in samples J15-2-S1a (S1 quartz vein; Fig.
630 9) and JSN17-4-HWb (HW quartz vein; Fig. 7), χ and δ in samples JSN29-1-S2c (S2
631 quartz vein; Fig. 8), JSN32-S1-QTZ-09 (S1 quartz vein; Fig. 9) and BC-CAN-09 (quartz
632 vein in the Canmet (Discovery) Zone, Fig. 16), χ and ε in samples BC-NV-09 (New Vein
633 Zone; Fig. 16) and MAP1-14 (surface shear zone; Fig. 13), or directly by component δ,
634 without evidence for component χ, as in samples J29-1/2-S2 (S2 quartz vein; Fig. 8),
635 JR20-25-BZb (Bonanza quartz vein; Fig. 12) and BF1750-5A (Zone E quartz vein; Fig.

636 13). β is sometimes the principal component of the white mica which were analysed, as in
637 samples JRPE-S2-QTZ-09 (S2 quartz vein; Fig. 8), BF1750-7A (Zone C shear zone; Fig.
638 15), BC70-3 (New Vein Zone, Fig. 16) and NW-DUM-5B (Fig. 13). β is also present as a
639 low-temperature component for sample BF1750-7C (Zone C quartz vein), in which it
640 seems to be aggregated with component α, both β and α components being subsequently
641 reworked by χ (Fig. 15).

642 Component χ is less well-expressed as compared to β, and yields ages clustering
643 around 2575 Ma. χ is detected as a high-temperature component of samples J25-HW-
644 QTZ-09 (HW quartz vein; Fig. 7) and BC-CAN-09 (Fig. 16). It is also frequently
645 observed in high-temperature steps and reworked by the δ, ε and sometimes φ
646 components in surface samples ADP-TOP-W, MAP5-35, MAP6-1 and SNBK-9B (Fig.
647 13) and in J25-WE-QTZ-09 and J15-2-WEa white micas from a quartz vein and related
648 shear zone of the WE structure (Fig. 11), in which it represents the oldest component. χ is
649 the main component in sample J25-HW-MYL-09 (Fig. 7), a shear zone hosting the HW
650 quartz vein, or in samples J15-2-S1a and JSN32-S1-QTZ-09 (Fig. 9), JSN17-4-HWb
651 (Fig. 7), JSN29-1-S2c (Fig. 8), MAP1-14 (Fig. 13), BC-NV-09 (Fig. 16), in which it is
652 superimposed on component β. Finally, χ is observed as a low temperature component, as
653 well as associated with partial recrystallization of components α and β within the white
654 micas from quartz veins sample from Zone C at the Beaufor mine (BF1750-7C; Fig. 15)
655 and from a S2 shear zone sample at Lac-Herbin (JRPE-S2-QTZ-09; Fig. 8).

656 Component δ is undoubtedly of major importance among the white mica analyses
657 performed during this study, suggesting that it could have had the strongest imprint. δ has
658 a mean age of c. 2551 Ma and is the only component that allowed the calculation of
659 plateau ages, at 2560.7 ± 3.3 Ma and 2549.0 ± 3.9 Ma, from samples J15-2-WEa (Fig.
660 11) and BF1750-5A (Fig. 15). Despite slight disturbances due to subsequent event
661 associated with component ε, δ is also the main and oldest component identified in the
662 age spectra of samples BF1750-5B (Zone E shear; Fig. 15) and BF1750-4 (Zone F quartz
663 vein; Fig. 15). Component δ is detected in high-temperature steps for a very large number
664 of analyses, and is affected to varying degrees by younger components ε and φ. This is
665 particularly well shown by mica samples of a S1 quartz vein (J15-2-S1b) and related

shear zone (JSN32-S1-MYL-09 and J25-8-S1) (Fig. 9). The same is true for all quartz vein samples of zones S3 (J29-1-S3, JSN25-4-S3b and J29-2-S2/S3; Fig. 10) and WE (J15-2-WEb and J25-WE-QTZ-09; Fig. 11). For S3 shear zone and quartz veins, it is the oldest component detected in their respective age spectra. Similar results are also found in quartz vein samples from surface exposure (SG-3; Fig. 13), and from the Beacon-2 and Beaufor mines (BC70-1A and BF1750-1D, respectively; Fig. 15 and 16). δ is only rarely observed in low temperature heating steps of age spectra, although it is clearly detected as such in sample JSN29-1-S2c (a S2 quartz vein; Fig. 8) and in two surface samples (quartz vein NW-DUM-5B and shear MAP1-14; Fig. 13).

Components ε and φ are mostly observed in low and intermediate temperature steps of age spectra. These are the two youngest components detected during this study, with mean ages of c. 2500 Ma for ε and c. 2452 Ma for φ. There are only two age spectra characterized by component ε in high-temperature steps, J30-S3 and J25-4-HW3 from shears S3 (Fig. 10) and HW3 (Fig. 12), respectively, which show no evidence for older components. The imprint of component ε is particularly well-detected in the intermediate temperature domain, and is a much stronger signal as compared to component φ.

When a large set of data is available, the use of probability density diagrams (frequency diagrams) is appropriate. As mentioned in section 4.1, frequency diagrams are used to determine the probability of occurrence of a given apparent age for each age sampled (at a 1 Ma frequency interval in our study), and provide a synthetic view of the distribution of apparent ages. Plateau and pseudo-plateau ages were compiled for the three studied mines and compared with the probability density diagrams of apparent ages (Figs. 14, 15 and 16). Hence, for the Lac-Herbin (Fig.14) and Beacon-2 mines, the probability density diagrams show a perfect age concordance for 5 of the 6 components mentioned above. With the exception of component φ, the age of components identified in these two mines is in agreement with frequency peaks of apparent ages as defined by their respective frequency diagrams (Figs. 14 and 15). The adequacy between validated ages and frequency peaks of apparent ages is less clear for the Beaufor mine, which can be due to a limited representativeness of the small number of samples from this mine.

While adequacy between the frequency peaks and the statistically validated ages (plateau and pseudo-plateau ages) is a factor of internal consistency and validation, the reverse is not a disqualifying factor. Biases can be induced by transition domain, within age spectra, between significant segments which will characterize distinct radiogenic components. This could be the case at the Lac Herbin mine for the two youngest components (φ and ε). Moreover, as the origin (partial recrystallization vs. aggregation) of the multiple radiogenic components present within a white mica grain governs the relations between them and thus the shape of the age spectra they generate (saddle or stepped shapes), it also controls the shape of the resulting frequency histograms. The high prevalence of partial recrystallization within the white mica from the Beaufor mine could explain the discrepancy between the estimated ages of components ε, δ, χ and β and the frequency peaks of apparent ages. This emphasizes the fact that a frequency histogram is not always a panacea, and that it must be handled with discernment and that data processing requires a careful degassing analysis and statistical validation by calculating plateau and pseudo-plateau ages.

Nevertheless, the age of the six components that were identified among the white mica spectrum are clearly distinct, with no overlaps (Fig. 17). They cover a time period of approximately 200 m.y., starting around c. 2651 Ma (component α), followed by 3 successive phases (components β, χ and δ) that peak with a period of c. 20-25 Ma at c. 2597 Ma (component β), 2575 Ma (component χ) and 2551 Ma (component δ), these three phases probably representing the paroxysm of hydrothermal activity since they left the strongest imprints in the study area. This is followed by two younger phases, associated with component ε ca. 50 m.y. later (at c. 2500 Ma) and component φ, another ca. 50 m.y. later (at c. 2452 Ma).

The errors attributed to the mean ages of the various components (Figs. 14, 15, 16 and 17) have no other meaning than standard deviations, because the age distributions observed for each component may be the expression of "analytical" dispersions as well as the duration of events.

6. DISCUSSION

6.1 Validation of $^{40}Ar/^{39}Ar$ ages

As most $^{40}Ar/^{39}Ar$ experiments, at least for white micas, suggest a mixing between different radiogenic components, one may question if the deconvolution of results is adequate. A systematic consistency between the ages of the distinct radiogenic components identified in amphibole and/or white mica grains suggests that it has been the case and this is the reason why some of them have been similarly labelled for different analyses. We think that this indicates that the ^{39}Ar–^{40}Ar age results have a regional geochronological and geological significance. Besides, the estimated age of component α (c. 2650 Ma) identified in white micas is consistent with the age of event #2 recorded by amphiboles (see Fig. 17), suggesting that the crystallization of this first generation of white micas in shear-related veins has been synchronous with the partial reset/recrystallization of amphiboles in the hosting rocks of the Bourlamaque pluton. The subsequent disturbing events preserved in white micas (i.e. components β to φ, from c. 2600 Ma down to c. 2450 Ma) are not recorded by amphiboles. On the other hand, the absence of components older than α in white micas, whether due to a complete obliteration or the non-existence of earlier components, precludes the establishment of genetic links between white micas and amphiboles prior to c. 2650 Ma, i.e. especially with respect to disturbance event #1 (c. 2667 Ma) recorded by amphiboles.

$^{40}Ar/^{39}Ar$ ages measured during this study cannot be attributed to the passive erosional exhumation of the AGB, in which case any given mineral species shall yield, within errors, the same range of ages, which is obviously not the case. Amphibole ages that cluster at ca. 2704 Ma overlap, within errors, with the U-Pb zircon age of the Bourlamaque pluton and are interpreted as magmatic cooling ages, close to crystallization (Figs. 6 and 17). Amphibole ages at c. 2667 Ma yielded by some plateau spectra and saddle-shaped perturbations can be attributed to regional peak metamorphism and/or syn-orogenic magmatism (Fig. 18), more likely coeval with the emplacement of the monzodioritic suite (2690-2670 Ma; e.g. Daigneault et al., 2002) of the Preissac-Lacorne batholith (Fig. 2). The partial or complete rejuvenation of $^{40}Ar/^{39}Ar$ amphibole ages with depth (over a vertical distance of approximately 300 metres) at Lac-Herbin (Fig. 6) is worthy of discussion. Obviously, these rejuvenating events, clustering at ca. 2665, 2650

and perhaps 2635 Ma (Fig. 6a), cannot be attributed to deformation since these amphibole samples were taken away from mineralized shear zones. We think that there are three possible explanations. (1) Age variations are due to progressive exhumation by erosion, and surface samples therefore crossed the Tc for amphibole earlier than those at depth. As argued above, this is unlikely since similar age-depth relations are not show by white mica samples. (2) There is an intrusive body at depth that is the cause of local thermal perturbations of the $^{40}Ar/^{39}Ar$ amphibole system; there is no geophysical and/or lithological evidence for shallow intrusions in either of the gold deposits hosted by the Bourlamaque pluton, and we thus consider that hypothesis as unlikely. (3) Amphibole spectrum perturbations are due to mineral recrystallization related to pervasive fluid impregnation, which would has been coeval with regional metamorphism and/or emplacement of monzodioritic (c. 2690-2670 Ma) and granitic (c.2660-2642 Ma) suites of the Preissac-Lacorne batholith, or both, an hypothesis that we prefer and which is more consistent with white mica results.

The $^{40}Ar/^{39}Ar$ analyses of white micas identified 5 radiogenic/mineral components whose mean ages decrease from c. 2600 Ma down to c. 2450 Ma. (Fig. 17). We believe that these ages are geologically significant because (1) white mica $^{40}Ar/^{39}Ar$ plateau and pseudo-plateau ages are consistent at the scale of the Bourlamaque pluton, i.e. similar plateau and pseudo-plateau ages were obtained in different deposits, (2) pairs of vein- and mylonite-hosted micas yielded overlapping plateau and pseudo-plateau ages, which is, for instance, consistent with the Sibson's et al. (1988) fault-valve model of coeval deformation and fluid circulation, and (3) there is very good consistency between the apparent age frequency peaks and the plateau and pseudo-plateau ages provided by samples from the Lac Herbin and Beacon-2 mines, but less so at the Beaufor mine for reasons mentioned above. The 5 identified components record sequential dissolution/recrystallization /neocrystallization/aggregation processes that affected white micas during at least 150 m.y., and that testify to dynamic recrystallization processes during peak periods of more-or-less intense fluid circulation and deformational events (Fig. 17). However, as discussed in the following section, the question remains regarding

784 the fertility of these hydrothermal events in terms of gold entrapment in associated
785 structures.
786
787 *6.2 Age and duration of gold-vein formation in the Val d'Or mining district*
788 The oldest evidence for fluid circulation in the Bourlamaque pluton is recorded by
789 amphiboles with ages within the age bracket inferred for the peak of regional
790 metamorphism and emplacement of the Preissac-Lacorne batholite, whereas the youngest
791 evidence is yielded by $^{40}Ar/^{39}Ar$ muscovite ages around 2450 Ma from quartz-veins
792 and/or hosting mylonites (Fig. 18). There is no magmatic muscovite in the Bourlamaque
793 pluton, and all muscovite/sericite minerals and/or aggregates analysed during this study
794 are related to fluid circulation/alteration driven by incremental shearing deformation.
795 Obviously, the development of quartz-carbonate-tourmaline vein systems hosted by the
796 Bourlamaque pluton has been also incremental. We cannot be sure that hydrothermal
797 fluids circulation generated during regional metamorphism (ca. 2670-2660 Ma) and/or
798 emplacement of the old (2690-2670 Ma) and young (2660-2642 Ma) plutonic suites of
799 the Preissac-Lacorne batholith, if any, has been coeval with the formation of auriferous
800 quartz veins. However, the identification of a radiogenic/mineral component of white
801 mica as old as c. 2650 Ma (Fig. 18) favors the onset of gold entrapment in the
802 Bourlamaque pluton (and the Val d'Or mining district *in extenso*) coeval, at the earliest,
803 with a corresponding hydrothermal stage referred to as α on Figure 18. Although the
804 progressive deformation and dynamic recrystallization induced by multiple hydrothermal
805 pulses precluded the preservation of most of the white mica that may have initially
806 crystallized concomitantly with the initiation of gold vein, say in the 2670-2660 Ma
807 range, we argue that gold vein formation occurred no earlier than c. 2650 Ma. In the Lac-
808 Herbin deposit, this component α would correspond to type 1 gold-bearing, aqueous-
809 carbonic fluid inclusions identified by Rezeau et al. (2017) which were generated,
810 according to them, during regional metamorphism.
811 Following the early stage α, $^{40}Ar/^{39}Ar$ muscovite ages define 4 other well-
812 expressed frequency peaks covering a time period of approximately 100 m.y. (Fig. 18), at
813 c. 2597 Ma (stage β), c. 2575 Ma (stage χ), c. 2551 Ma (stage δ), c. 2500 Ma (stage ε),

and a more discrete one at c. 2452 Ma (stage φ). The spreading of $^{40}Ar/^{39}Ar$ ages from c. 2650 Ma down to c. 2500 Ma (Fig. 18) suggests that localized shear deformation and related gold mineralization and/or remobilization in the Val d'Or mining district may have lasted for more than 150 m.y., which is significantly longer than suggested in current literature. At the Lac-Herbin deposit, Rezeau et al. (2017) identified three unrelated fluid inclusion types in the main vein filling ore stage, (1) aqueous-carbonic inclusions interpreted to have formed during regional metamorphism (corresponding to our component α) and to represent gold-bearing fluids, (2) barren high-temperature, aqueous, moderately saline inclusions postdating type 1 inclusions, and considered as a remobilizing agent of earlier precipitated gold, and (3) barren low-temperature, aqueous, high saline inclusions similar to crustal brines reported throughout the Canadian Shield and considered to be unrelated to orogenic gold mineralization (e.g. Boullier et al., 1998). The age of fluid inclusions studied by Rezeau et al. (2017) is unknown and, since the sampled structures are not identified in their study, it is impossible to make any connection with $^{40}Ar/^{39}Ar$ data from the Lac-Herbin deposit. Interestingly, Rezeau et al. (2017) argued that type 2 fluid inclusions represent a different hydrothermal fluid emplaced after and at higher temperature (as compared to type 1), that acted as a remobilizing agent for previously precipitated gold. They suggested that these fluids were generated during and/or following the emplacement of S-type granitic intrusions of the Preissac-Lacorne batholith at ca. 2645-2611 Ma. This is basically consistent with our genetic model of multistage tectonothermal events, and we suggest that gold introduction/remobilization continued for a long time period after the final stages of post-orogenic magmatism, most probably due to a slow cooling rate of the Archean lithosphere (e.g. Willigers et al., 2002; and references below).

Our $^{40}Ar/^{39}Ar$ results are consistent with other geochronological evidence for «young» Au-rich hydrothermal fluid circulation that have been obtained with different isotopic tools in the Val d'Or mining district and adjacent areas of the southern Abitibi Belt (Fig. 18). Gold mineralization ages of 2633 ± 3 Ma, 2627 ± 2 Ma and 2600 ± 3 Ma have been obtained by U-Pb dating of hydrothermal rutile, sphene and titanite, respectively, at the Camflo mine (Jemielita et al., 1990; Zweng et al., 1993). In the Sigma

mine, Wong et al. (1991) measured a U-Pb age of 2599 ± 9 Ma on a hydrothermal rutile. Sm-Nd analyses of scheelite and tourmaline from Sigma, Perron and Sisco deposits yielded isochron ages of 2596 ± 33 Ma and 2593 ± 18 Ma (Anglin et al., 1996), whereas Olivo et al. (2007) measured a Pb-Pb age of 2566 ± 71 Ma from hydrothermal pyrites in the Sisco deposit. Hanes et al. (1992) reported a $^{40}Ar/^{39}Ar$ muscovite age of 2579 ± 9 Ma from a quartz-tourmaline vein at the Sigma mine, arguing that this was a minimal age for mineralization. Zweng et al. (1993) argued that these $^{40}Ar/^{39}Ar$ ages record closure during post-2640 Ma cooling but, according to Corfu (1993), it is also possible that some of the observed age variations record late and localized pulses of hydrothermal activity. Moreover, Sasseville and Jebrak (2017) recently measured $^{187}Re/^{187}Os$ isochrons clustering at c. 2575, c. 2505, c. 2398 and c. 2267 Ma from various gold deposits of the Val d'Or area, the latter two age clusters being tentatively attributed to thermal pulses and gold remobilization related to the Matachewan Igneous Province.

At the scale of the Superior Province, there is accumulating geochronological evidence for major crustal deformation event(s) and related metamorphism spreading over a timeframe much larger than suggested in literature (e.g. Percival (2007), for instance), that described the Superior Province as a succession of five orogenic events which propagated southward from 2.72 to 2.68 Ga. In Ontario, Easton (2000) argued that the distribution of metamorphic grade and age of metamorphism reflects a series of tectonic events between 2710 and 2640 Ma, which followed the early accretion (between 2720 and 2690 Ma) of different oceanic terranes (arcs, back-arcs) and microcontinents. Such a time interval (2710-2640 Ma) is in agreement with U-Pb zircon age constraints for metamorphism, syn-orogenic magmatism and deformation in the Val d'Or mining district (Fig. 18). It is also consistent with $^{40}Ar/^{39}Ar$ age data from the northern Abitibi Belt and the adjacent Opatica Plutonic Belt (OPB) where amphibole and micas ages record a metamorphic history starting at c. 2685 Ma and vanishing around 2630 Ma (Daoudene et al., 2014; 2016). To the north of the OPB, in the Opinaca subprovince, granulite-facies regional metamorphism spreads over ages varying from c. 2666 Ma to 2636 Ma (Morfin et al., 2013). Metamorphism even lasted down to ca. 2620-2600 Ma in supracrustal rocks of the La Grande subprovince (Fontaine et al., 2017; 2018). Combined with

874 geochronological data from the southern Abitibi belt, this is a strong indication that peak
875 and duration of regional metamorphism have been more-or-less coeval over a large
876 region, if not all over the Pontiac, Abitibi and Opatica subprovinces and beyond.
877
878 *6.3 Tectonic implications for Archean orogenic gold deposits.*
879 In the Superior Province of Ontario, Easton (2000) suggested that relationships
880 between subprovince type, metamorphic grade and geochronological ages show that
881 granite-greenstone domains (such as the AGB) preserves old greenschist- to lower-
882 amphibolite-facies metamorphic event(s) whereas high-grade gneiss domains (such as the
883 OPB) preserves the youngest metamorphic events. This was interpreted to be consistent
884 with a «deep-later» model of gold mineralization (e.g. Stüwe, 1998), in which gold-
885 bearing fluids and pegmatite-forming melts develop, at least in part, during prograde
886 granulite-facies metamorphism/magmatism (and devolatilization) in the lower crust and
887 are structurally-trapped (as «post-metamorphic» quartz veins and dikes) during ascension
888 to shallow crustal levels (see also Krogh, 1993). Presently, there are not sufficiently
889 abundant and largely distributed metamorphic age data in the Quebec Superior Province
890 to support Easton's (2000) proposition. Metamorphic grade variations in the AGB (Faure,
891 2015) indicates, however, that metamorphic isograds increase progressively from the
892 uppermost towards the lowermost crustal sequences of both the Abitibi and Opatica belts;
893 orthogneisses of the Opatica Plutonic Belt (OPB) are at amphibolite- to granulite-facies
894 (Sawyer and Benn, 1993; Daoudene et al., 2016) whereas the lower part of the AGB is at
895 amphibolite facies and its uppermost sequences at greenschist- and lower grade,
896 indicating that metamorphism increases with crustal depth (Daoudene et al., 2016;
897 Tremblay et al., 2019). Faure's (2015) metamorphic compilation also indicates that
898 metamorphic isograds are essentially subhorizontal in the AGB, in which higher-grade
899 metamorphic rocks occur within and around TTG complexes that essentially represent
900 structural windows exposing OPB-like lower crust orthogneisses.
901 An increasing volume of continental crust and crustal fluid production towards the
902 end of the Archean (e.g. Condie et Benn, 2006; Sizova et al., 2010) and a higher
903 geothermal gradient and fluid convection efficiency can have accounted for multiple, ~10

m.y.-long peaks of hydrothermal activity in the Val d'Or mining district (Fig. 18). Connolly (2010), for instance, argued that metamorphic fluids in the crust are expelled by hydrothermal pulses/batches along fracture/fault zones, which is conceptually consistent with the sequence of frequency peaks of $^{40}Ar/^{39}Ar$ ages highlighted for the Bourlamaque pluton. It is therefore reasonable to propose that the time periodicity of hydrothermal pulses recorded by our $^{40}Ar/^{39}Ar$ data is a direct consequence of physical processes responsible for the formation of these vein systems, although we cannot be sure that every hydrothermal pulse has been recorded. A succession of tens to thousands of hydrothermal pulses over a period of 100 m.y., or more, implies the incremental and repetitive precipitation and/or remobilization of auriferous sulphides and native gold. Incidentally, several gold occurrences of the Val d'Or district preserve evidence for multiple generations of gold influx within a single deposit (Robert and Brown, 1986; Robert and Kelly, 1987; Roussy, 2003; Olivo et al., 2006; Rezeau et al., 2017).

As mentioned above, in the Val d'Or mining camp, the Cadillac tectonic zone (CTZ) is currently considered as a 1st-order structure that drained hydrothermal fluids towards 2nd- and 3rd-order shears (e.g. Neumayr et al., 1999) such as the ones hosting gold mineralization in the Bourlamaque pluton. Do our $^{40}Ar/^{39}Ar$ data mean that faulting increments along the CTZ continued to be active long after the end of regional metamorphism (i.e. post-ca. 2630 Ma)? Is it reasonable to infer more-or-less localized hydrothermal and faulting activity along the CTZ during 150 m.y., if not more? The CTZ is a 250 km-long high-strain zone (Fig. 2) that had a complex structural evolution with successive shortening, extensional and late strike-slip faulting events (e.g. Daigneault et al., 2002). Bedeaux et al. (2017) published a very detailed structural analysis of the Rouyn-Val d'Or segment of the CTZ, arguing that the latest dextral strike-slip fault increments occurred at c. 2665 Ma and were coeval with the emplacement of major orogenic gold deposits, such as those of the Val d'Or district. Their timing hypothesis is, however, poorly constrained as it basically relies on selected isotopic ages from the Val d'Or area (as compiled by Robert et al., 2005) and on U-Pb dating of the syn-kinematic Murdock Creek and Lebel stocks in the Kirkland Lake area, Ontario (Wilkinson et al., 1999), 200 km west of the Val d'Or district. Long-lasting faulting and variations of the

kinematic frame of a single crustal-scale structure are common; for instance, the Alpine, San Andreas and North Anatolian faults, which are often used as modern equivalents to the CTZ, have been active since c. 25, 30 and 43 m.y., respectively (Lamb, 2011; Popov et al., 2012; Nuriel et al., 2019). These are minimal values for the duration of deformation along these crustal faults. The North Anatolian fault, for instance, is a long-lived fault system that formed during multiple events and by reactivation of pre-existing fault systems, the present dextral style of deformation being active since at least 11 m.y. (Nuriel et al., 2017).

Finally, it is worth discussing the implications of the $^{40}Ar/^{39}Ar$ dating of auriferous structures of the Bourlamaque pluton for the relative timing of barren veins and east-west trending brittle faults that cut across gold mineralization at each of the studied deposits, i.e. the Perron, Beaufor, New Vein, Beacon and Lac Herbin-Sud faults (see Fig. 5). We emphasize here that these faults expose fabrics that contrast sharply with gold-related structures, as they are essentially characterized by brittle to brittle-ductile deformation features, sub-horizontal lineations, and bear no evidence for intense hydrothermal activity during faulting. Such structures also exist elsewhere in the Val d'Or mining district as, for instance, the K-Zone at the Siscoe deposit (Sauvé et al., 1993) and the Dunraine shear (Daigneault, 1996; Moorehead et al., 1998) which fringes the Louvicourt massive sulfide deposit. The orientation and structural characteristics of shear zones and late brittle faults preserved in the Bourlamaque pluton are reminiscent of regional tectonics in the Val-d'Or mining district where the CTZ show evidence for both reverse and dextral strike-slip movement, attributed to different increments of faulting (Bedeaux et al., 2017) or dextral transpression during progressive deformation (Robert, 1989). Fault structures within the studied gold deposits suggest, however, that reverse and dextral trancurrent faulting are genetically unrelated and probably resulted from sequential faulting. After an undetermined period of time following gold mineralization, long enough to annihilate significant fluid circulation and allow the transition to brittle conditions of deformation, strike-slip faulting was initiated in the Val d'Or mining district and various sets of faults, crosscutting the pre-existing shears and veins, were formed. If correct, this means that strike-slip fault formation and/or reactivation has been

964 coeval with or younger than ca. 2500-2450 Ma (latest Archean) hydrothermal events.
965 Interestingly, Kaminemi et al. (1990) described similar brittle structures and cataclastic
966 faults with Rb/Sr ages of 2300 Ma (Early Proterozoic) cutting Late Archean granitic
967 plutons in the western Superior Province; they argued that this is evidence that structural
968 disturbance of the internal Superior craton did not terminate with plutonism at the end of
969 the Kenoran orogeny but continued intermittently for at least several hundred millions
970 years, possibly in response to events taking place beyond margins of that craton.
971
972 **7. CONCLUSION**
973 The large amount of $^{40}Ar/^{39}Ar$ analyses produced during this study has raised
974 important implications to be made on the different veins and shear structures that were
975 sampled. The whole geochronological dataset obviously reflects the final state of the
976 different auriferous shear zones systems. Hydrothermal components expressing previous
977 states potentially existed before being obliterated, as it is the case for component α (c.
978 2650 Ma) which has been only locally detected and almost totally erased by intense
979 hydrothermal/tectonic activity at c. 2600-2550 Ma (Fig. 18). In the Lac-Herbin deposit,
980 the preserved hydrothermal history started around c. 2600 Ma with the crystallization of
981 component β along most structures, at the exception of WE and HW3 which may have
982 been initiated later, around 2575 Ma and 2500 Ma, respectively (Fig. 14). The activity of
983 structure S2 seems to have ceased as early as c. 2550 Ma, whereas S3 would have formed
984 at that time and continued until c. 2450 Ma. S1 records almost continuous hydrothermal
985 activity between c. 2600 Ma and c. 2450 Ma, for a longer period than HW, WE and
986 Bonanza, which seem to become static at c. 2500 Ma (Fig. 14). As suggested by Figure
987 17, multiplying the number of samples and $^{40}Ar/^{39}Ar$ analyses at the Beaufor and Beacon-
988 2 deposits would have conducted most likely to a similar interpretation regarding their
989 structural and hydrothermal evolution. $^{40}Ar/^{39}Ar$ ages measured in gold deposits of the
990 Bourlamaque pluton can be thus attributed to a succession of structurally-driven
991 hydrothermal events rather than to the passive cooling of the dated minerals. Such
992 hydrothermal events were obviously not continuous but corresponded to ca. 10-to-20
993 m.y. pulses of distributed deformation and related fluid circulation.

The hydrothermal and deformational evolution depicted by Figure 18 is not obviously limited to the Bourlamaque pluton and there has been probably a similar succession of hydrothermal events in other auriferous quartz-carbonate-tourmaline vein systems of the Val d'Or mining district. If correct, this means that these orogenic gold deposits were formed much later than usually proposed in literature and for a time length of more than 150 m.y., during the incremental deformation of alternating, seismically active segments of crustal faults systems along which episodic flow is associated with fluid pressure cycling and episodic fluid redistribution. Such a duration of crustal faulting appears to be much longer than documented in modern crustal-scale fault settings such as the San Andreas and the North-Anatolian fault zones along which deformation proceeds since up to 40 m.y, which is, however, a minimum value since deformation and faulting are still active today. Such a long duration of crustal faulting in the Abitibi Greenstone Belt, can be tentatively attributed to the geodynamic context of the Archean, with higher geothermal gradients and weak lithospheres in which competent layers are limited to a thin brittle crust that favour distributed strains, as documented in a number of Precambrian terranes (e.g. Choukroune et al., 1995; Chardon et al., 2008; Cagnard et al., 2007; Gapais et al., 2009), as well as by analogue and numerical modeling in which horizontal flow of the lower ductile crust combines with distributed shortening of the upper brittle crust (e.g. Cagnard et al., 2006; Cruden et al., 2006; Rey and Houseman, 2006; Gray and Pysklywec, 2010). As a consequence, Precambrian belts tend to show much slower cooling rates than modern ones (e.g. Willigers et al., 2002), and long-lasting magmatic and deformation histories of the order of 100 Ma or more with rather steady kinematic frameworks (e.g. Gapais et al., 2005; Chardon and Jayananda, 2008; Taylor et al., 2020).

Declaration of Competing Interest.

The authors declare that they have no known competing financial interests or personal relationships that could have appeared to influence the work reported in this paper.

Acknowledgements

The Natural Science and Engineering Council of Canada (NSERC) has provided research grants to A. Tremblay (NSERC-PG105669). This contribution is part of Jérémie Lemarchand (JL) PhD thesis at the Université du Quebec à Montreal (UQAM). JL benefited of financial support from BMP-Innovation (FQRNT/NSERC) and DIVEX grants. We sincerely thank E.J. Cowan and an anonymous reviewer, as well as the associate editor, O. Kreuzer, for critical comments that improved the manuscript. Thanks to C. Gobeil and D. Vermette of Alexis Minerals Inc. for help and support for field work in the Lac-Herbin mine and the Val d'Or area. Thanks are also due to M. Laithier, A. Desaulniers and M. Perrot for drawing the figures.

References

Alexandrov, P., Ruffet, G. and Cheilletz, A., 2002. Muscovite recrystallization and saddle-shaped $^{40}Ar/^{39}Ar$ age spectra: examples from the Blond granite (Massif Central, France). Geochimica et Cosmochimica Acta 66: 793–1807.

Anglin, C.D., Jonasson, I.R., and Franklin, J.M., 1996. Sm-Nd dating of scheelite and tourmaline; implications for the genesis of Archean gold deposits, Val d'Or, Canada. Economic Geology 91: 1372-1382.

Bedeaux, P., Pilote, P., Daigneault, R., and Rafini, S., 2017. Synthesis of the structural evolution and associated gold mineralization of the Cadillac Fault, Abitibi, Canada. Ore Geology Reviews 82: 49-69.

Berryman, K.R., Cochran, U.A., Clark, K.J., Biasi, G.P., Langridge, R.M., and Villamor, P., 2012. Major earthquakes occur regularly on an isolated plate boundary fault. Science 336: 1690-1693.

Boullier, A.-M., Firdaous, K., and Robert, F., 1998. On the significance of aqueous fluid inclusions in gold-bearing quartz vein deposits from the southeastern Abitibi subprovince (Québec, Canada). Economic Geology 93: 216-223.

Bosse, V., Feraud, G., Ruffet, G., Ballevre, M., Peucat, J.-J., and De Jong, K., 2000. Late Devonian subduction and early-orogenic exhumation of eclogite-facies rocks from the Champtoceaux Complex (Variscan belt, France). Geological Journal 35: 297-325.

Cagnard, F., Gapais, D. and Barbey, P., 2007. Collision tectonics involving juvenile crust: the example of the southern Svecofennides. Precambrian Research 154: 125–141.

Cagnard, F., Brun, J.P. and Gapais, D., 2006. Modes of thickening of analogue weak lithospheres. Tectonophysics, 421: 145–160.

1060 Castonguay, S., Ruffet, G., and Tremblay, A. 2007. Dating polyphase deformation across
1061 low-grade metamorphic belts: an example based on $^{40}Ar/^{39}Ar$ muscovite age
1062 constraints from the southern Quebec Appalachians, Canada. Geological Society
1063 of America Bulletin 119: 978-992.
1064 Castonguay, S., Ruffet, G., Tremblay, A., and Féraud, G., 2001. Tectonometamorphic
1065 evolution of the southern Quebec Appalachians: $^{40}Ar/^{39}Ar$ evidence for
1066 Ordovician crustal thickening and Silurian exhumation of the internal Humber
1067 zone. Geological Society of America Bulletin 113: 144–160.
1068 Chardon, D. and Jayananda, M., 2008. Three-dimensional field perspective on
1069 deformation, flow and growth of the lower continental crust (Dharwar craton,
1070 India). Tectonics, 27, TC 1014. doi:10.1029/2007TC002120.
1071 Chardon, D., Jayananda, M., Chetty, T.R.K. and Peucat, J.-J., 2008. Precambrian
1072 continental strain and shear zone patterns: south Indian case. Journal Geophysical
1073 Research 113, B08402. doi:10.1029/2007JB005299.
1074 Cheilletz, A., Ruffet, G., Marignac, C., Kolli, O., Gasquet, D., Féraud, G., and Bouillin,
1075 J.P., 1999. $^{40}Ar/^{39}Ar$ dating of shear zones in the Variscan basement of the Greater
1076 Kabylia (Algeria). Evidence of an Eo-Alpine event at 128 Ma (Hauterivian–
1077 Barremian boundary): geodynamic consequences. Tectonophysics 306: 97–116.
1078 Choukroune, P., Bouhallier, H. and Arndt, N.T., 1995. Soft lithospheres during periods of
1079 Archaean crustal growth or crustal reworking. In: Early Precambrian Processes
1080 (M.P. Coward and A. Ries, eds). Geological Society Special Publication 95: 67–
1081 86.
1082 Ciborowski, J., Kerr, A., Ernst, R.E., McDonald, I., Minifie, M.J., Harlan, S.S., and
1083 Millar, I. 2015. The Early Proterozoic Matachewan Large Igneous Province:
1084 Geochemistry, Petrogenesis, and Implications for Earth Evolution. Journal of
1085 Petrology 56: 1459-1494.
1086 Corfu, F. 1993. The evolution of the Southern Abitibi Greenstone Belt in light of precise
1087 U-Pb geochronology. Economic Geology 88: 1323-1340.
1088 Condie, K.C., and Benn, K. 2006. Archean Geodynamics: Similar to or Different from
1089 Modern Geodynamics? American Geophysical Union, Geophysical
1090 Monograph164, p. 47-59.
1091 Connolly, J.A.D. 2010. The mechanics of metamorphic fluid expulsion. Elements 6:
1092 165-171.
1093 Couture, J.-F., Pilote, P., Machado, N., and Desrochers, J.-P., 1994, Timing of gold
1094 mineralization in the Val-d'Or camp, southern Abitibi belt: Evidence 2020for two
1095 distinct mineralization events. Economic Geology 89: 1542–1551.
1096 Cowan, E.J. 2020. Deposit-scale structural architecture of the Sigma-Lamaque gold
1097 deposit, Canada – insights from a newly proposed 3D method for assessing
1098 structural controls from drill hote data. Mineralium Deposita 55: 217-240.
1099 Cox, S.F. 2005. Coupling between deformation, fluid pressures, and fluid flow in

ore-producing hydrothermal systems at depth in the crust. Economic Geology 100th Anniversary Volume, pp. 39–75.

Cox, S.F., Knackstedt, M.A., and Braun, J. 2001. Principles of structural control on permeability and fluid flow in hydrothermal systems. Society of Economic Geologist Review 14: 1-24.

Cox, S.F, Etheridge, M.A., and Wall, V.J. 1987. The role of fluids in syntectonic mass transport, and the localization of metamorphic vein-type ore deposits. Ore Geology Reviews 2: 65-86.

Cruden, A.R., Nasseri, M.H. and Pysklywec, R., 2006. Surface topography and internal strain variation in wide hot orogens from three-dimensional analogue and two-dimensional numerical vice models; analogue and numerical modelling of crustal-scale processes. Geological Society Special Publication 253: 79–104.

Dahl, P.S., 1996. The effects of composition on retentivity of argon and oxygen in hornblende and related amphiboles: a field-tested empirical model. Geochimica Cosmochimica Acta 60 : 3687–3700.

Daigneault, R. 1983. Géologie et géochimie du gisement d'or de la mine Lamaque, Val d'Or, Québec. Mémoire de maîtrise, École polytechnique de Montréal, Québec, Canada.

Daigneault, R., 1996. Couloirs de déformation de la sous-Province de l'Abitibi: Ministère des Ressources Naturelles du Québec MB 96-33, 115 p.

Daigneault, R., Mueller, W., and Chown, E. 2002. Oblique Archean subduction: accretion and exhumation of an oceanic arc during dextral transpression, Southern Volcanic Zone, Abitibi Subprovince Canada. Precambrian Research 115: 261-290.

Daoudene, Y., Leclerc, F., and Tremblay, A. 2016. Une histoire tectono-métamorphique commune et de longue durée pour les sous-provinces d'Abitibi et d'Opatica, Province du Supérieur, Québec, Canada. Ministère de l'Énergie et des Ressources naturelles, Québec; MB 2016-01, 43 pages.

Daoudene, Y., Tremblay, A., Ruffet, G. and Leclerc, F. 2014. Étude structurale et métamorphique de la bordure nord-est de la Ceinture de roches vertes de l'Abitibi, Québec, Canada : apport de la thermochronologie $^{40}Ar/^{39}Ar$ et implications tectoniques. Ministère des Ressources et de la Faune, Québec.

Deckart, K., Feraud, G., and Bertrand, H., 1997. Age of Jurassic continental tholeiites of French Guyana/Suriname and Guinea: implications to the opening of the Central Atlantic Ocean. Earth and Planetary Science Letters 150: 205–220.

Deino A., Potts, R. 1992.Age-probability spectra for examination of single-crystal $^{40}Ar/^{39}Ar$ dating results: examples from Olorgesailie, southern Kenya rift. Quaternary International 13/14: 47-53.

De Putter, T. and Ruffet, G., 2020. Supergene manganese ore records 75 Myr-long

Campanian to Pleistocene geodynamic evolution and weathering history of the Central African Great Lakes region - Te–tonic drives, climate assists. Gondwana Research 83: 96-117.

De Putter, T., Ruffet, G., Yans, J., and Mees, F. 2015. The age of supergene manganese deposits in Katanga and its implications for the Neogen evolution of African Great Lakes Region. Ore Geology Reviews 71: 350-362.

Dimroth, E., Imreh, L., Goulet, N., and Rocheleau, M., 1983, Evolution of the south-central segment of the Archean Abitibi belt, Quebec. Part II: Tectonic evolution and geomechanical model: Canadian Journal of Earth Sciences 20: 1355–1373.

Dodson, M.H. 1973. Closure temperature in cooling geochronological and petrological systems. Contributions to Mineralogy and Petrology 40: 259-274.

Dubé, J. 2018. Caractérisation métallogénique et structurale de la minéralisation aurifère des gisements Triangle et Cheminée No. 4, Val d'Or, Abitibi, Québec. Mémoire de maîtrise, Université du Québec à Chicoutimi, Québec, Canada.

Ducharme, Y., Stevenson, R.K. and Machado, N. 1997. Sm-Nd geochemistry and U-Pb geochronology of the Preissac and La Motte leucogranites, Abitibi Subprovince; Canadian Journal of Earth Sciences 34: 1059–1071.

Dunlap, W.J., 1997. Neocrystallization or cooling? $^{40}Ar/^{39}Ar$ ages of white micas from low-grade mylonites. Chemical Geology 143: 181–203.

Easton, R.M. 2000. Metamorphism of the Canadian Shield, Ontario, Canada. I. The Superior Province. The Canadian Mineralogist 38: 287-317.

Faure, S. 2015. Relations entre les minéralisations aurifères et les isogrades métamorphiques en Abitibi. Rapport. Projet CONSOREM 2013-03. 52 p.

Feng, R., Kerrich, R., McBride, S. and Farrar, E. 1992. $^{40}Ar/^{39}Ar$ age constraints on the thermal history of the Archean Abitibi greenstone belt and the Pontiac subprovince: implications for terrane collision, differential uplift, and overprinting of gold deposits. Candian Journal of Earth Sciences 29: 1389-1411.

Fleck, R.J., Sutter, J.F., and Elliot, D.H., 1977. Interpretation of discordant $^{40}Ar/^{39}Ar$ age spectra of Mesozoic tholeiites from Antarctica. Geochimica Cosmochimica Acta 41 : 15-32.

Fontaine, A., Dubé, B., Malo, M., Doucet, D. 2018. Geology of the Chechoo gold property, Eeyou Istchee Baie-James, Superior Province, northern Quebec. Geological Survey of Canada, Open File 8403, 24 pages.

Fontaine,A., Dubé, B., Malo, M., Ravenelle, J.-F., Fournier, E., McNicoll, V., Beausoleil, C., Prud'homme, and N. Goutier, J. 2017. The Éleonore gold mine: exploration, discovery and understanding of an emerging gold district in Eeyou Estchee LJames Bay, Superior Province, nprthern Québec, Canada. In «Proceedings of Exploration 17: Sixth Decennial International Conference on Mineral Exploration, edited by V. Tschirhart and M.D. Thomas, p. 601-617.

1178 Fortier, S. M. and Gilettit B. J., 1989. An empirical model for predicting diffusion
1179 coefficients in silicate minerals. Science 245: 1481 - 1484.
1180 Gapais, D., Cagnard, F., Gueydan, F., Barbey, P., and Ballèvre, M. 2009. Mountain
1181 building and exhumation processes through time: inferences from nature and
1182 models. Terra Nova 21: 188-194.
1183 Gapais, D., Potrel, A., Machado, N. and Hallot, E., 2005. Kinematics of long-lasting
1184 Paleoproterozoic transpression within the Thompson Nickel Belt (Manitoba,
1185 Canada). Tectonics 24,TC3002; doi: 10.1029/2004TC001700.
1186 Goldfarb, R.J., Groves, D.I., and Gardoll, S. 2001. Orogenic gold and geologic time: a
1187 global synthesis. Ore Geology Reviews 18: 1-75.
1188 Groves, D.I., Goldfarb, R.J., Knox-Robinson, C.M., Ojala, J., Gardoll, S., Yun, G.Y., and
1189 Holyland, P. 2000. Late-kinematic timing of orogenic gold deposit and significance for
1190 computer-based exploration techniques with emphasis on the Yilgarn Block,
1191 Western Australia. Ore Geology Reviews 17: 1-38.
1192 Groves, D.I., Goldfarb, R.J., Gebre-Mariam, M., Hagemann, S.G., and Robert, F. 1998.
1193 Orogenic gold deposits: a proposed classification in the context of their crustal
1194 distribution and relationships to other gold deposit types. Ore Geology Reviews
1195 13: 7-27.
1196 Gray, R. and Pysklywec, R.N., 2010. Geodynamic models of Archean continental
1197 collision and the formation of mantle lithosphere keels. Geophysical Research
1198 Letters 37: 1-5.
1199 Hames, W. E., Cheney, J. T. and Tracy, R. J., 2008. Single-crystal $^{40}Ar/^{39}Ar$ age variation
1200 in muscovite of the Gassetts Schist and associated gneiss, Vermont Appalachians.
1201 American Mineralogist 93: 384-395.
1202 Hanes, J.A., Archibald, D.A., Hogson, C.J., and Robert, F. 1992. Dating of Archean
1203 auriferous quartz vein deposits in the Abitibi Greenstone Belt, Canada. 40Ar/39Ar
1204 evidence for a 70-100 Ma time gap between plutonism-metamorphism and
1205 mineralization. Economic Geology 87: 1849-1861.
1206 Harrison, T.M., Célérier, J., Aikman, A.B., Hermann, J., and Heizler, M.T. 2009.
1207 Diffusion of ^{40}Ar in muscovite. Geochimica Cosmochimica Acta 73: 1039–1051.
1208 Hubert, C., 1990. Geological framework, evolution and structural setting of gold and base
1209 metal deposits of the Abitibi greenstone belt, Canada. Univeristy of Western
1210 Australia Short Courses Notes 24, p. 53–62.
1211 Jäger, E., Niggli, E., and Wenk, E., 1967. Rb–Sr Altersbestimmungen an Glimmern der
1212 Zentralalpen. Beiträge zur Geologischen Karte der Schweiz, Neue Folge 134, 67
1213 pages.
1214 Jemielita RA, Davis DW, and Krogh TE. 1990. U-Pb evidence for Abitibi gold
1215 mineralization postdating greenstone magmatism and metamorphism. Nature 346:
1216 831–834.
1217 Jourdan, F., and Renne, P. R. (2007). Age calibration of the Fish Canyon sanidine

$^{40}Ar/^{39}Ar$ dating standard using primary K–Ar standards. Geochimica et Cosmochimica Acta 71(2): 387-402.

Jourdan, F., Verati, C., and Féraud, G. (2006). Intercalibration of the Hb3gr $^{40}Ar/^{39}Ar$ dating standard. Chemical Geology, 231(3): 177-189.

Kamber, B.S., Blenkinsop, T.G., Villa, I.M., and Dahl, P.S., 1995. Proterozoic transpressive deformation in the Northern Marginal Zone, Limpopo Belt, Zimbabwe. Journal of Geology 103: 493–508.

Kamineni, D.C., Stone, D., and Peterman, Z.E., 1990. Early Proterozoic deformation in the western Superior Province. Geological Society of America Bulletin 102: 1623-1634.

Kerrich, R. and Cassidy, K.F. 1994. Temporal relationships of lode gold mineralization to accretion, magmatism, metamorphism and deformation - Archean to present – a review. Ore Geology Review 9 : 263-310.

Krogh, T.E., 1993. High precision U-Pb ages for granulite metamorphism and deformation in the Archean Kapuskasing structural zone, Ontario: implications for structure and development of the lower crust. Earth and Palnatary Science Letters 119: 1-18.

Lamb, S. 2011. Cenozoic tectonic evolution of the New Zealand plate-boundary zone : a paleomagnetic perspective. Tectonocphysics 509, 135-164.

Lemarchand, J. 2012. Les minéralisations filoniennes aurifères de pluton de Bourlamaque (Val d'Or, Abitibi) : synthèse structurale et apport de la datation $^{40}Ar/^{39}Ar$. Ph.D. thesis. Université du Québec à Montréal-Université de Rennes 1.

Ludden, J., Hubert, C., and Gariepy, C., 1986, The tectonic evolution of the Abitibi greenstone belt of Canada. Geological Magazine 123: 153–166

Malo, M., Ruffet, G., Pincivy, A., and Tremblay, A., 2008. A $^{40}Ar/^{39}Ar$ study of oceanic and continental deformation processes during an oblique collision: Taconian orogeny in the Quebec reentrant of the Canadian Appalachian. Tectonics 27: 1–29.

Moorehead, J., Tremblay, A., Pelz, P., and Beaudoin, G., 1998. Géologie de la mine Louvicourt, in Pilote, P., Moorhead, J., and Mueller, W., eds., Développement d'un arc volcanique, la région de Val-d'Or, Ceinture de l'Abitibi - Volcanologie physique et évolution métallogénique: Association Géologique du Canada Guide d'excursion A-2, p. 39–58.

Morasse, S., 1998, Geology, structure and timing of gold mineralization at the Kiena deposit, Val d'Or, Québec: Unpublished Ph.D. thesis, Kingston, ON, Queen's University.

Morfin, S., Sawyer, E.W., and Bandyayera, D. 2013. Large volumes of anatectic melt retained in granulite facies migmatites: an injection complex in northern Quebec. Lithos 168-169: 200-218.

1257 Mortensen, J.K. and Card, K.D., 1993, U-Pb age constraints for the magmatic and
1258 tectonic evolution of the Pontiac subprovince. Canadian Journal of Earth Sciences
1259 30: 1970–1980.
1260 Neumayr, P., Hagemann, S.G., and Couture, J.-F., 1999, Structural setting, textures, and
1261 timing of hydrothermal vein systems in the Val d'Or camp, Abitibi, Canada:
1262 Implications for the evolution of transcrustal, second- and third-order fault zones
1263 and gold mineralization: Canadian Journal of Earth Sciences 37: 95–114.
1264 Nuriel, P., Craddock, J., Kylander-Clark, A.R.C., Tonguç Uysal, I., Karabacak, V., Dirik,
1265 R.K., Harcker, and B.R., Weinberger, R. 2019. Reactivation history of the North
1266 Anatolian fault zone based on calcite age-strain analuses. Geology 47: 465-469.
1267 Olivo GR, Isnard H, Williams-Jones AE, and Gariépy C. 2007. Pb isotope compositions
1268 of pyrite from the C quartz-tourmaline vein of the Siscoe gold deposit, Val d'Or,
1269 Quebec: constraints on the origin and age of the gold mineralization. Economic
1270 Geology 102: 137–146.
1271 Olivo, G.R., Chang, F., and Kyser, T.K. 2006. Formation of the auriferous and barren
1272 North Dipper veins in the Sigma mine, Val d'Or, Canada: Constraints from
1273 structural, mineralogical, fluid inclusion, and isotopic data. Economic Geology
1274 101: 607 - 631.
1275 Passchier, C.W., and Trouw, R.A.J., 1996, Micro-tectonics: Berlin Heidelberg, Springer-
1276 Verlag Editions, 289 p.
1277 Percival, J. 2007. Geology and metallogeny of the Superior Province. Canada. In W. D.
1278 Goodfellow (ed). Mineral Deposits of Canada: A Synthesis of Major Deposit-
1279 Types District Metallogeny, the Evolution of Geological Provinces, and
1280 Exploration Methods. Geological Association of Canada, Mineral Deposits
1281 Division, Special Publication, p. 903-928
1282 Pitra P., Ballèvre M. and Ruffet G. (2010). Inverted metamorphic field gradient towards a
1283 Variscan suture zone (Champtoceaux Complex, Armorican Massif, France).
1284 Journal of Metamorphic Geology 28/2, 183-208.
1285 Popov, A.A., Sobolev, S.V., and Zoback, M.D. 2012. Modeling evolution of the San
1286 Andreas Fault system in northern and Central California. Geochemistry,
1287 Geophysics, Geosystems (G^3) 13, doi. 10.1029/2012GC004086.
1288 Powell, W.G., Hodgson, C.J., Hanes, J.A., Carmichael, D.M., McBride, S., and Farrar,
1289 E., 1995, 40Ar-39Ar geochronological evidence for multiple postmetamorphic
1290 hydrothermal events focused along faults in the southern Abitibi greenstone belt:
1291 Canadian Journal of Earth Sciences 32: 768–786.
1292 Renne, P.R., Balco, G., Ludwig, R.L., Mundil, R., and Min, K., 2011. Response to the
1293 comment by W.H. Schwarz et al. on "Joint determination of ^{40}K decay constants
1294 and $^{40}Ar*/^{40}K$ for the Fish Canyon sanidine standard, and improved accuracy for
1295 $^{40}Ar/^{39}Ar$ geochronology" by PR Renne et al. (2010). Geochimica et
1296 Cosmochimica Acta, 75: 5097-5100.

Renne, P.R., Mundil, R., Balco, G., Min, K., and Ludwig, R.L., 2010. Joint determination of ^{40}K decay constants and $^{40}Ar*/^{40}K$ for the Fish Canyon sanidine standard, and improved accuracy for $^{40}Ar/^{39}Ar$ geochronology. Geochimica et Cosmochimica Acta 74: 5349–5367.

Rey, P. and Houseman, G., 2006. Lithospheric scale gravitational flow: the impact of body forces on orogenic processes from Archaean to Phanerozoic. In: Analogue and Numerical Modelling of Crustal-Scale Processes (S. Buiter and G. Schreurs, eds). Geological Society Special Publicaation, 253: 153–167.

Rezeau, H., Moritz, R., and Beaudoin, G., 2017. Formation of Archean batholith-hosted gold veins at the Lac Herbin deposit, Val d'Or district, Canada: mineralogical and fluid inclusion constraints. Mineralum Deposita 52: 421-442. DOI 10.1007/s00126-016-0669-5.

Robert, F. 2001. Syenite-associated disseminated gold deposits in the Abitibi greenstone belt, Canada. Mineralium Deposita, 36(6): 503-516.

Robert, F., 1989. Internal structure of the Cadillac tectonic zone, southeast of Val-d'Or, Abitibi greenstone belt, Quebec: Canadian Journal of Earth Sciences 26: 2661–2675.

Robert, F. 1990, Structural setting and control of gold-bearing quartz veins of the Val-d'Or area, southeastern Abitibi subprovince: University of Western Australia Short Course Notes 24, p. 167–210.

Robert, F. 1994, Vein fields in gold districts: Example of Val-d'Or, southeastern Abitibi subprovince, Québec: Geological Survey of Canada Paper 94-1C, p. 295–302.

Robert, F., and Brown, A.C. 1986. Archean gold-quartz veins at the Sigma mine, Abitibi Greenstone Belt, Quebec: Part I. Geological relations and formation of the vein system. Part II. Vein paragenesis and hydrothermal alteration. Economic Geology 81: 578-616.

Robert, F., and Kelly, W.C. 1987. Ore-forming fluids in Archean gold-bearing quartz veins at the Sigma mine, Abitibi Greenstone Belt, Quebec, Canada. Economic Geology 82: 1464-1482.

Robert, F., Poulsen, K.H., Cassidy, K.F., and Hodgson, C.J. 2005. Gold metallogeny of the Superior and Yilgarn cratons. Economic Geology 100th Anniversary Volume, pp. 1001–1033.

Roddick, J. 1983. High precision intercalibration of ^{40}Ar-^{39}Ar standards. Geochimica et Cosmochimica Acta, 47(5): 887-898.

Roddick, J.C., Cliff, R. A. and Rex, D. C., 1980. The evolution of excess argon in alpine biotites - $^{40}Ar/^{39}Ar$ analysis: Earth Planetary Science Letters 48: 185-208.

Roussy, J. 2003. Relations entre la distribution de l'or, la structure, la composition des veines et de l'altération hydrothermale à la mine Beaufor, Val d'Or, Québec. M.Sc. thesis, Laval University, 311 pages.

Ruffet, G., Féraud, G., Balèvre, M., and Kiénast, J.-R., 1995. Plateau ages and excess

argon in phengites: an ^{40}Ar–^{39}Ar laser probe study of Alpine micas (Sesia Zone, Western Alps, northern Italy). Chemical Geology 121: 327–343.

Ruffet, G., Féraud, G., and Amouric, M., 1991. Comparison of ^{40}Ar–^{39}Ar conventional and laser dating of biotites from the North Trégor Batholith. Geochimica and Cosmochimica Acta 55: 1675–1688.

Ruffet, G., Gruau, G., Ballèvre, M., Féraud, G., and Philippot, P. 1997. Rb/Sr and $^{40}Ar/^{39}Ar$ laser probe dating of high-pressure phengites from the Sesia zone (Western Alps): underscoring of excess argon and new age constraints on the high-pressure metamorphism. Chemical Geology 141: 1-18.

Sauvé, P., Imreh, L., and Trudel, P., 1993. Description des gîtes d'or de la région de Val-d'Or: Ministère des Ressources Naturelles du Québec MM 91-03, 178 p.

Sasseville, C., and Jebrak, M. 2017. Gold epichrons in the Abitibi greenstone belt, Canada, and the impact of early Proterozoic Matachewan LIP event.

Sawyer, E.W., and Benn, K. 1993. Structure of the high-grade Opatica Belt and the adjacent low-grade Abitibi Subprovince, Canada: an Archean mountain front. Journal of Structural Geology 15: 1443-1458.

Scharer, K., Weldon II, R., Streig, A., and Fumal, T. 2014. Paleoearthquakes at Frazier Mountain, California delimit extent and frequency of pas San Andreas Fault ruptures along 1857 trace. Geophysical Research Lettres 41: 4527-4534.

Scott, C.R., Mueller, W.U., and Pilote, P. 2002. Physical volcanology, stratigraphy, and lithogeochemistry of an Archean volcanic arc: evolution from plume-related volcanism to arc rifting of SE Abitibi Greenstone Belt, Val-d'Or, Canada. Precambrian Research 115: 223-260.

Sheldon, H.A., and Ord, A. 2005. Evolution of porosity, permeability and fluid pressure in dilatant faults post-failure: implications for fluid flow and mineralization. Geofluids 5: 272-288.

Sibson, R.H., 2001. Seismogenic framework for hydrothermal transport and ore deposition. Reviews in Economie Geology 14: 25-50.

Sibson, R.H., Robert, F., and Poulsen, K.H., 1988, High-angle reverse faults, fluid-pressure cycling, and mesothermal gold-bearing quartz deposits: Geology 16: 551–555.

Sizova, E., Gerya, T., Brown, M., and Perchuk, L.L. 2010. Subduction styles in the Precambrian: Insight from numerical experiments. Lithos 116: 209-229.

Stuwe, K. 1998. Tectonic constraints on the timing relationships of metamorphism, fluid production and gold-bearing quartz vein emplacement. Ore Geology Reviews 13: 219-228.

Taner, M. F., and Trudel, P. 1989. Bourlamaque batholith and it's gold potential, Val d'Or, Québec. CIM Bulletin 82: 33-42.

Tartese, R. and Boulvais, P., 2010. Differentiation of peraluminous leucogranites "en route" to the surface. Lithos 114: 353-368.

1377 Tartese, R., Ruffet, G., Poujol, M., Boulvais, P., and Ireland, T. R. 2011. Simultaneous
1378 resetting of the muscovite K-Ar and monazite U-Pb geochronometers: A story of
1379 fluids. Terra Nova 23: 390–398.
1380 Taylor, R.J.M., Johnson, T.E., Clark, C., and Harrison, R.J. 2020. Persistence of melt-
1381 bearing Archean lower crust for >200 m.y. – an example from the Lewisian
1382 Complex, northwest Scotland. Geology 48: 221-225.
1383 Tessier, A.C., 1990, Structural evolution and host rock dilation during emplacement of
1384 gold- bearing quartz veins at Perron deposit, Val-d'Or, Quebec: Unpublished
1385 M.S. thesis, Kingston, ON, Queen's University, 242 p.
1386 Tremblay, A. 2001. Post-mineralization faults in the Beaufor gold deposit, Abitibi
1387 Greenstone Belt, Canada: geometry, origin and tectonic implications for the Val
1388 d'Or mining district. Economic Geology 96: 509-524.
1389 Tremblay, A., Ruffet. G. and Bédard. J.H. 2011. Obduction of Tethyan-type ophiolites –
1390 a case-study from the Thetford-Mines ophiolitic Complex, Québec Appalachians,
1391 Canada. Lithos 125: 10-26.
1392 Tremblay, A., Daoudene, Y., Ruffet, G. and Leclerc, F. 2019. The Abitibi-Opatica
1393 contacts, Archean Superior Province (Quebec) – is it a tectonic plate boundary
1394 suture? GAC-MAC meeting, Québec city, Canada.
1395 Turner, G., Huneke, J.C., Podose, F.A., and Wasserbrug, G.J., 1971. $^{40}Ar/^{39}Ar$ ages and
1396 cosmic ray exposure ages of Apollo 14 samples. Earth and Planetary Science
1397 Letters 12: 19–35.
1398 Villa, I.M. 2010. Disequilibrium textures versus equilibrium modelling: geochronology at
1399 the crossroads; in Spalla, M. I., Marotta, A. M. & Gosso, G. (eds) Advances in
1400 Interpretation of Geological Processes: Refinement of Multi-scale Data and
1401 Integration in Numerical Modelling. Geological Society, London, Special
1402 Publications 332, 1–15.
1403 Villa, I.M., 1998. Isotopic closure. Terra Nova 10 : 42–47.
1404 West, D.P., Jr., and Lux, D.R., 1993. Direct dating of mylonitization by the $^{40}Ar/^{39}Ar$
1405 method: An example from the Norumbega fault zone, Maine: Earth and Planetary
1406 Science Letters 120: 221-237.
1407 Williamson, K., 2001. Analyse structurale des zones aurifères et chronologie des
1408 évènements géologiques à la mine Beacon-2. Laval Université (Quebec), M.Sc.
1409 thesis, 111 pages.
1410 Willigers, J.A., van Gool, J.A.M., Wijbrans, J.R., Krogstad, E.J., and Mezger, K. 2002.
1411 Posttectonic cooling of the Nagssugtoqidian Orogen and a comparison of
1412 contrasting cooling histories in Precambrian and Phanerozoic orogens. The
1413 Journal of Geology 110: 503-517.
1414 Wilkinson, L., Cruden, A.R., and Krogh, T.E. 1999. Timing and kinematics of post-
1415 Temiskaming deformation within the Larder Lake-Cadillac deformation zone,

southwest Abitibi greenstone belt, Ontario, Canada. Candian Journal of Earth Science 36: 627-647.

Wong, L., Davis, D.W., Krogh, T.E., and Robert, F., 1991, U-Pb zircon and rutile geochronology of Archean greenstone formation and gold mineralization in the Val-d'Or region, Quebec: Earth and Planetary Science Letters 104: 325–336.

Zweng, P.L., Mortensen, J.K., and Dalrymple, G.B. 1993. Thermochronology of the Camflo gold deposit, Malartic, Quebec: implications for magmatic underplathing and the formation of gold-bearing quartz veins. Economic Geology 88: 1700-1721.

Figure captions

Figure 1. Diagram P_f-ε-t. Diagram illustrating the concept of incremental deformation within the fault-valve model of Sibson et al. (1988), and the relationships between fluid pressure (Pf) and strain rate (ε) fluctuations with time (t).

Figure 2. Simplified geological map of the southern Abitibi Greenstone Belt (Abitibi supprovince) and adjacent Pontiac subprovince. BP, Bourlamaque pluton; LP. Lacorne pluton; PP, Preissac pluton; LMP, La Motte pluton; FP, Flavrian pluton; LLCfz, Larder Lake-Cadillac fault zone; DPMfz, Destor-Porcupine-Manneville fault zone. Modified from Bedeaux et al. (2017).

Figure 3. Geological map of the Val d'Or area and location of the principal vein-type orogenic gold deposits (black dots) of the Val d'Or mining district. See Figure 1 for location.

Figure 4. Cross-section of the Lac-Herbin gold deposit showing the location of the principal mineralized and barren shear zones. Red, main mineralized shear zones; Yellow, subsidiary mineralized shear zones, Black, barren shear zone. Modified from Lemarchand (2012).

Figure 5. Synthetic North-South profiles of mineralized shear zones (red) and crosscutting brittle faults (green) for the Lac-Herbin (a), Beaufor (b) and Beacon-2 (c) mines. Note that almost all the mineralized shear zones shown in red also correspond to mined stopes at each deposit. Modified from Lemarchand (2012).

Figure 6. Single-grain $^{39}Ar/^{40}Ar$ results for amphiboles for the Lac-Herbin mine. (a) Density probability diagrams (frequency diagram) of apparent ages and validated ages (plateau and pseudo-plateau – see text for explanation). (b) Validated ages (plateau and pseudo-plateau – see text for explanations) versus depth. (c), (d), (e), (f), (g), (h) and (i) Amphibole $^{40}Ar/^{39}Ar$ age spectra. Apparent age error bars are at the 1σ level; errors in the J-parameter are not included. Plateau and pseudo-plateau ages (1σ uncertainties including errors in the J-parameter) are given when applicable. See text for explanations. (J) Mean values of the significant segments of the $^{37}Ar_{Ca}/^{39}Ar_K$ (# Ca/K) spectra versus depth. See section 5.1 for explanations.

Figure 7: Analysed white micas from the HW zone of the Lac-Herbin mine (see Fig. 4 for

location) with conventional age spectra (apparent ages vs. $\%^{39}Ar_K$), $^{40}Ar^*$ degassing spectra ($(^{40}Ar/\Delta VT°)/(^{40}Ar/\Delta VT°)_{Max}$ vs. $\%^{39}Ar_K$), weighted age spectra (apparent ages vs. $\%((^{39}Ar_K/\Delta VT°)/(^{39}Ar_K/\Delta VT°)_{Max})$ and resized age spectra (steps of 4% of $^{39}Ar_K$ released). See text for explanations. Plateau and pseudo-plateau ages (1σ uncertainties including errors in the J-parameter) are given when applicable. Also shown is the frequency diagram of apparent ages of resized age spectra (see text for explanation). VT°, the laser power control voltage, is a proxy indicator of temperature.

Figure 8. Analysed white micas from the S2 zone of the Lac-Herbin mine. See caption of Figure 7 and section 5.2.2 for explanations.

Figure 9. Analysed white micas from the S1 zone of the Lac-Herbin mine. See caption of Figure 7 and section 5.2.2 for explanations.

Figure 10. Analysed white micas from the S3 zone of the Lac-Herbin mine. See caption of Figure 7 and section 5.2.2 for explanations.

Figure 11. Analysed white micas from the WE zone of the Lac-Herbin mine. See caption of Figure 7 and section 5.2.2 for explanations.

Figure 12. Analysed white micas from the HW3 zone of the Lac-Herbin mine. See caption of Figure 7 and section 5.2.2 for explanations.

Figure 13. Analysed white micas from surface samples of the Lac-Herbin mine. See caption of Figure 7 and section 5.2.2 for explanations.

Figure 14. Synthesis of the validated ages of Lac-Herbin mine (plateau and pseudo-plateau) obtained on white micas from quartz veins (circles) and shears (squares), grouped by zones (HW, S1, S2, S3, WE, HW3, Bonanza, Flat and surface) superimposed on the probability density diagram of the resized apparent ages. See text for explanation. The red arrows show the sequences of successive components identified during the analysis of the same white mica. White circles or squares represent unvalidated ages.

Figure 15. Analysed white micas from the Beaufor mine. See captions of Figure 7 and 14, and section 5.2.2 for explanations.

Figure 16. Analysed white micas from the Beacon 2 mine. See captions of Figure 7 and 14, and section 5.2.2 for explanations.

Figure 17. Synthesis of the validated ages (plateau and pseudo-plateau) of the Bourlamaque pluton obtained on amphiboles (triangles) and on white micas (quartz veins as circles and shears as squares) versus depth, superimposed on the probability density diagram of apparent ages. White circles or squares represent unvalidated ages.

Figure 18. Synthetic diagram showing the distribution of amphibole and white mica ^{39}Ar-^{40}Ar ages obtained during this study, and compilation of the time range of U-Pb and $^{40}Ar/^{39}Ar$ ages measured on different lithologies and for metamorphism in the Val d'Or area, including geochronological data for different gold mines and mining districts of the southern Abitibi Belt (extracted from Powell et al., 1995). Each black line represents a single plateau or sub-plateau $^{40}Ar/^{39}Ar$ age (including the error range) measured during this study; green for amphiboles and yellow for white micas.

Genetic links between peak metamorphism and vein-type Au mineralization are debate.

$^{40}Ar/^{39}Ar$ data indicate long-lasting and sequential hydrothermal activity.

Au-rich fluids circulation started around 2650 Ma in the Bourlamaque pluton.

Hydrothermal pulses continued for more than 150 m.y., possibly down to c. 2450 Ma.